

# Parametric study and scaling of a minijet-manipulated supersonic jet

Changhao Tan<sup>1,†,‡</sup>, Arun Kumar Perumal<sup>2,‡</sup> and Yu Zhou<sup>3,1,†</sup>

<sup>1</sup>Center for Turbulence Control, Harbin Institute of Technology, Shenzhen 518055, PR China

<sup>2</sup>Jet Acoustics and Flow-Control Laboratory, Department of Aerospace Engineering, Indian Institute of Technology Kanpur, Kanpur 208016, India

<sup>3</sup>School of Mechanics and Mechanical Engineering, College of Engineering, Eastern Institute of Technology, 315000 Ningbo, PR China

(Received 2 April 2024; revised 8 September 2024; accepted 9 September 2024)

This work aims to perform a parametric study on a round supersonic jet with a design Mach number  $M_d = 1.8$ , which is manipulated using a single steady radial minijet with a view to enhancing its mixing. Four control parameters are examined, i.e. the mass flow rate ratio  $C_m$  and diameter ratio  $d/D$  of the minijet to main jet, and exit pressure ratio  $P_e/P_a$  and fully expanded jet Mach number  $M_j$ , where  $P_e$  and  $P_a$  are the nozzle exit and atmospheric pressures, respectively. Extensive pressure and schlieren flow visualization measurements are conducted on the natural and manipulated jets. The supersonic jet core length  $L_c/D$  exhibits a strong dependence on the four control parameters. Careful scaling analysis of experimental data reveals that  $L_c/D = f_1(C_m, d/D, P_e/P_a, M_j)$  may be reduced to  $L_c/D = f_2(\xi)$ , where  $f_1$  and  $f_2$  are different functions. The scaling factor  $\xi = J(d_i/D_j)/(\gamma M_j^2 P_e/P_a)$  is physically the penetration depth of the minijet into the main jet, where  $J(d_i/D_j)$  is the square root of the momentum ratio of the minijet to main jet ( $d_i$  and  $D_j$  are the fully expanded diameters of  $d$  and  $D$ , respectively),  $\gamma$  is the specific heat ratio and  $\gamma M_j^2 P_e/P_a$  is the non-dimensional exit pressure ratio. Important physical insight may be gained from this scaling law into the optimal choice of control parameters such as  $d/D$  and  $P_e/P_a$  for practical applications. It has been found for the first time that the minijet may induce a street of quasi-periodical coherent structures once  $C_m$  exceeds a certain level for a given  $P_e/P_a$ . Its predominant dimensionless frequency  $St_e (\equiv f_e D_j/U_j)$  scales with a factor  $\zeta = J(d_i/D_j) \sqrt{\gamma M_j^2 P_e/P_a}$ , which is physically the ratio of the minijet momentum thrust to the ambient pressure thrust. The formation mechanism of the street and its role in enhancing jet mixing are also discussed.

**Key words:** supersonic flow, mixing enhancement, jets

† Email addresses for correspondence: [yuzhou@eitech.edu.cn](mailto:yuzhou@eitech.edu.cn), [18s153681@stu.hit.edu.cn](mailto:18s153681@stu.hit.edu.cn)

‡ Joint first authors.

## 1. Introduction

Control of high-speed jets has been extensively studied over the past few decades due to its wide range of engineering applications, such as mixing enhancement, noise suppression, infrared reduction, ejector-thrust augmentation and thrust vectoring (Gutmark, Schadow & Yu 1995; Knowles & Saddington 2006; Cattafesta & Sheplak 2011). Various techniques for manipulating supersonic jets have been developed in the past and can be passive and active. Passive methods, e.g. non-circular nozzles, modified lips and tabs, are widely used due to their easy implementation and high cost-effectiveness (Gutmark et al. 1995; Knowles & Saddington 2006). However, being characterized by permanent fixtures, they are often only effective in a limited range of operating conditions and may not always produce desirable effects. For example, the passive control optimized to reduce noise during aircraft take-off and landing may lead to thrust loss during cruise (Seifert, Theofilis & Joslin 2004). On the other hand, active techniques can be applied when needed, thus limiting thrust loss only during their activation, and may produce a drastic effect on manipulated jets (Cattafesta & Sheplak 2011).

One of the frequently used active techniques for the manipulation of high-speed jets is fluidic injection, also referred to as minijets, secondary jets and air tabs. This technique has been demonstrated to be quite successful in controlling high subsonic and supersonic jets (e.g. Krothapalli, Strykowski & King 1998; Ibrahim, Kunimura & Nakamura 2002; Coderoni, Lyrintzis & Blaisdell 2018; Semlitsch *et al.* 2019), thus attracting a great deal of attention in the literature. There are many parameters associated with minijets, which may produce a profound influence on control performance, including the operating nozzle pressure ratio (*NPR*) ( $= P_{0s}/P_a$ , where  $P_{0s}$  and  $P_a$  are the stagnation pressure at the nozzle inlet and atmospheric pressure, respectively), the minijet injection angle  $\theta$  with respect to main stream, the number  $N$  of minijets, the injection pressure ratio (*IPR*) ( $= P_{0s,i}/P_a$ , where  $P_{0s,i}$  is the stagnation pressure at the minijet inlet), the diameter ratio  $d/D$ , velocity ratio  $U_i/U_j$  and mass flow rate ratio  $C_m$  of the minijet to main jet. In his pioneering work, Davis (1982) studied the effect of  $d/D$  ( $= 1/8$  and  $1/16$ ) on the mixing characteristics of a Mach number ( $M$ ) 0.8 jet manipulated using two minijets. He discovered that, given  $C_m$ , a minijet of a smaller  $d/D$  may penetrate deeper into main jet, thus being more effective in manipulating the jet. To study the effect of *IPR* on jet mixing, Cuppoletti & Gutmark (2014) experimentally manipulated a design Mach number ( $M_d$ ) 1.56 jet in the over-expanded ( $NPR = 2.5$ ) and under-expanded ( $NPR = 4.5$ ) regimes using 24 minijets at  $IPR = 2.5\text{--}4.5$ . For a given *NPR*, jet mixing was enhanced with increasing *IPR* or  $U_i/U_j$ , which was accompanied by increasing  $C_m$ . Semlitsch *et al.* (2019) extended this work to a larger *IPR* range (2–8) using 12 minijets and found that an increase in *IPR* was associated with a deep penetration of the minijet into the main jet. Despite numerous previous investigations, there is a lack of systematic study on various control parameters such as  $U_i/U_j$ ,  $d/D$ , *IPR* and  $C_m$ , which interweave and influence each other.

Recently, Perumal & Rathakrishnan (2022) manipulated a jet of  $M_d = 2$  via  $N = 2$  minijets ( $d/D = 1/13$ ) and found empirically that supersonic core length  $L_c^* = L_c/D$ , a quantitative indicator of jet mixing, scales with  $\sqrt{MR}/(\gamma M_j^2 P_e/P_a)$ , where  $MR$  is the total momentum ratio of the minijet to main jet and  $\gamma$ ,  $M_j$  and  $P_e/P_a$  are the specific heat ratio, fully expanded jet Mach number and exit pressure ratio, respectively. In this paper, an asterisk denotes normalization by  $D$ . Khan *et al.* (2022) extended this scaling law to  $N = 3, 4, 6$  minijets on a jet of  $M_d = 1.5$ , and proposed a revised scaling factor, i.e.  $\sqrt{MR_N}/(\gamma M_j^2 P_e/P_a)$ , where  $MR_N$  is the momentum ratio of the individual minijet to main jet. However, neither Perumal & Rathakrishnan (2022) nor Khan *et al.* (2022) studied

supersonic jets manipulated by a single minijet notwithstanding the fact that the control performance of  $N = 1$  may be better than that of  $N \geq 2$  (Perumal & Zhou 2021). Then, whether their developed scaling laws could be valid for the case of  $N = 1$  has yet to be confirmed. Furthermore, previous studies on the effect of  $d/D$  on jet mixing are focused on the manipulation of subsonic jets (Davis 1982; Perumal, Verma & Rathakrishnan 2015, Perumal & Zhou 2018, Perumal *et al.* 2022). To the authors' best knowledge, this effect has never been documented for supersonic jet manipulation. Naturally, one may raise a question as to the robustness of the developed scaling laws for varying  $d/D$ . For a practical device such as an aircraft jet engine, the minijet would be drawn probably from the flow entering the nozzle, implying an  $IPR$  would not exceed the  $NPR$  (Henderson 2010). Thus, can we predict the optimal  $d/D$  from the scaling law for maximized jet mixing given the limiting scenario of  $IPR = NPR$ ?

This study sets out to address the issues raised above, along with associated flow physics. Thus, the present work embarks on the systematic experimental study of an  $M_d = 1.8$  jet manipulated by a single minijet with various  $d/D$  and  $P_e/P_a$ , covering the over-expanded and perfectly expanded states. The jet mixing quantification is done through detailed Pitot pressure measurement and the flow structure of the manipulated jet is analysed through high-speed schlieren images captured along the injection and non-injection planes of the jet. The paper is organized as follows. Section 2 presents experimental details. The flow characteristics of the natural jet are briefly discussed in § 3, which is then followed by documenting the effect of  $C_m$  and  $d/D$  at various  $P_e/P_a$  and  $M_j$  on jet mixing in § 4. A new scaling law is proposed based on experimental data. The effect of the minijet on thrust vectoring is also investigated in § 5. Section 6 presents the finding of a street of quasi-periodical structures and scaling of its predominant frequency. This work is concluded in § 7.

## 2. Experimental details

### 2.1. Supersonic jet rig and control minijet

A schematic of the supersonic jet rig is given in figure 1. Air is compressed by a compressor and stored in three air tanks connected in series, with a total storage capacity of  $8 \text{ m}^3$  at a pressure of 12 bar. The compressed air from the storage tanks passes through pressure regulators and control valves before entering a plenum chamber. The chamber consists of a diffuser with a half-angle of  $15^\circ$  and a cylindrical settling chamber of 114 mm in diameter and 400 mm in length. The contraction section from 114 mm at the end of the settling chamber to 20 mm is the same as used in Perumal & Zhou (2018), whose contour is given by  $D/2 = 57 - 47 \sin^{1.5}[\pi/2 - 9(x + L)/8 * \pi/180]$ , where  $L$  ( $= 30.68$  mm) is the nozzle length. The required pressure in the settling chamber is achieved via a pressure regulating valve and is measured using a gauge transducer (MEAS M3234) with a pressure range of 0–7 bar. Two wire-mesh screens are placed at the diffuser and the settling chamber, respectively, to reduce the turbulence intensity. The nozzle mounted at the end of the contraction section can be replaced to obtain different design conditions.

An axisymmetric converging–diverging nozzle is used to generate a jet of  $M_d = 1.8$ . The converging section contracts from  $D_1 = 20$  mm at the end of the contraction section to  $D_{th} = 8.34$  mm at the throat, following a fifth-order polynomial function, i.e.  $(D(x) - D_{th})/(D_1 - D_{th}) = 1 - 10[(x + L)/L_1]^3 + 15[(x + L)/L_1]^4 - 6[(x + L)/L_1]^5$  (Zhang & Fan 2003), where  $L_1$  ( $= 18$  mm) is the length of the converging section. The

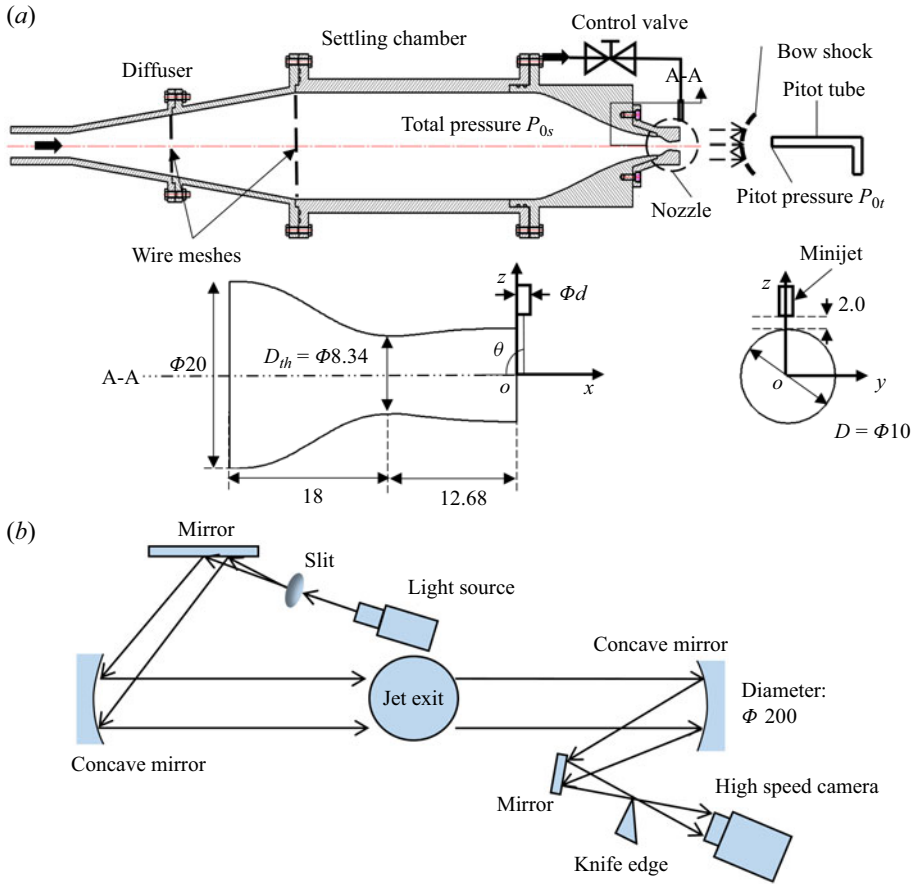


Figure 1. Schematics of (a) supersonic jet facility and (b) schlieren flow visualization measurement. All lengths are in mm.

diverging section is designed based on the method of characteristics presented in Zucrow & Hoffman (1976) from  $D_{th}$  to the nozzle exit diameter  $D = 10$  mm.

A control minijet is issued from a stainless steel tube with an inner diameter  $d$ , whose axis is 0.15–0.25 mm downstream of the nozzle exit. Following Davis (1982), the tube exit is 2 mm away from the nozzle lip along the  $z$  direction so that the interference between the issuing minijet and the spreading shear layer of main jet can be minimized. Six different tubes are used, resulting in  $d/D = 1/20, 1/9.5, 1/7.7, 1/6.5, 1/5.3$  and  $1/4.1$ . The minijet comes from another chamber where the required pressure is separately maintained.

## 2.2. Flow conditions

The stagnation temperature  $T_0$  of main jet and minijet is as ambient temperature  $T_a$  ( $= 300$  K), i.e.  $T_0/T_a = 1$ . The  $NPR$  is from 3 to 6 for both natural and manipulated jets. The nozzle is calibrated following Akram, Perumal & Rathakrishnan (2021), and the design  $NPR$ , i.e.  $NPR_d$ , as determined from the isentropic equation is 5.75 for the jet of  $M_d = 1.8$ . Then,  $NPR < NPR_d$  and  $NPR > NPR_d$  correspond to the over- and under-expanded states, respectively. Parameters  $M_j$  and  $P_e/P_a$  are related via the isentropic

$NPR$	$T_0/T_a$	$M_d$	$M_j$	$P_e/P_a$	$U_j$ (m s <sup>-1</sup> )	$Re$ ( $\times 10^5$ )
3	1	1.8	1.36	0.52	403	4.52
4			1.56	0.70	443	5.80
5			1.71	0.87	471	6.94
6			1.83	1.05	491	7.98

Table 1. Flow conditions for the natural jet of design Mach number  $M_d = 1.8$ .

relations:

$$M_j = \left[ (NPR^{(\gamma-1)/\gamma} - 1) \frac{2}{\gamma - 1} \right]^{0.5}, \quad (2.1)$$

$$\frac{P_e}{P_a} = \left( \frac{1 + \frac{\gamma - 1}{2} M_j^2}{1 + \frac{\gamma - 1}{2} M_d^2} \right)^{\gamma/(\gamma-1)}, \quad (2.2)$$

where  $\gamma = 1.4$  for air. From (2.1)–(2.2), the over- and under-expanded states of the jet correspond to  $M_j < M_d$  or  $P_e/P_a < 1$  and  $M_j > M_d$  or  $P_e/P_a > 1$ , respectively. The velocity of the main jet may be calculated from the following equation:

$$U_j = \sqrt{\frac{2\gamma}{\gamma - 1} RT_0 \left[ 1 - \left( \frac{1}{NPR} \right)^{(\gamma-1)/\gamma} \right]}, \quad (2.3)$$

where  $R = 287 \text{ J kg}^{-1} \text{ K}^{-1}$  is the gas constant for air. The Reynolds numbers  $Re = \rho_j D U_j / \mu_j$  of the jet at the minimum and maximum  $NPR$  or  $M_j$  are  $4.5 \times 10^5$  and  $8.0 \times 10^5$ , respectively, where the jet density  $\rho_j$  is determined from

$$\rho_j = \left( \frac{NPR \times P_a}{RT_0} \right) / \left( 1 + \frac{\gamma - 1}{2} M_j^2 \right)^{1/(\gamma-1)}, \quad (2.4)$$

and  $\mu_j$  is the viscosity calculated based on Sutherland’s formula (Anderson, Tannehill & Pletcher 1984). Table 1 lists  $NPR$ ,  $M_j$ ,  $U_j$ ,  $P_e/P_a$  and other parameters of interest.

The  $IPR$  varies from 2 to 8 and  $C_m = \dot{m}_i / \dot{m}_j$  is between 0.18 % and 11.87 % for various  $d/D$  (table 2), where  $\dot{m}_i$  and  $\dot{m}_j$  are the minijet and main jet mass flow rates, respectively. Both  $\dot{m}_i$  and  $\dot{m}_j$  are calculated from the isentropic equations:

$$\dot{m}_i = 0.6847 \frac{P_{0s,i} A_i}{\sqrt{RT_0}}, \quad (2.5)$$

$$\dot{m}_j = 0.6847 \frac{P_{0s} A_j}{\sqrt{RT_0}}, \quad (2.6)$$

where  $A_i = \pi d^2 / 4$  and  $A_j = \pi D_{th}^2 / 4$ . The mass flow rate of a jet calculated from inviscid compressible flow theory would be close to its actual mass flow rate if the nozzle diameter exceeds 0.35 mm (Jindra 1970). The present minimum  $d$  is 0.5 mm. Furthermore, both minijet and main jet are choked ( $IPR > 1.89$  and  $NPR > 1.89$ ) so that (2.5)–(2.6) can be

$T_0/T_a = 1$	IPR													
	$C_m$ (%)	2	2.5	3	3.5	4	4.5	5	5.5	6	6.5	7	7.5	8
1/20	0.18	0.22	0.27	0.31	0.36	0.40	0.45	0.49	0.54	0.58	0.63	0.67	0.72	
1/9.5	0.79	0.99	1.19	1.39	1.59	1.78	1.98	2.18	2.38	2.58	2.77	2.97	3.17	
1/7.7	1.21	1.52	1.82	2.13	2.43	2.73	3.04	3.34	3.64	3.95	4.25	4.56	4.86	
1/6.5	1.73	2.16	2.59	3.02	3.45	3.89	4.32	4.75	5.18	5.61	6.04	6.48	6.91	
1/5.3	2.60	3.24	3.89	4.54	5.19	5.84	6.49	7.14	7.79	8.43	9.08	9.73	10.38	
1/4.1	4.31	5.39	6.47	7.55	8.63	9.71	10.79	11.87	—	—	—	—	—	

Table 2. Mass flow rate ratio  $C_m$  of minijet to main jet for various IPRs at exit pressure ratio  $P_e/P_a = 0.70$  ( $NPR = 4$ ).

used to calculate  $\dot{m}_i$  and  $\dot{m}_j$ . The velocity  $U_i$  and fully expanded Mach number  $M_i$  of the minijet can be estimated from

$$U_i = \sqrt{\frac{2\gamma}{\gamma - 1} RT_0 \left[ 1 - \left( \frac{1}{IPR} \right)^{(\gamma-1)/\gamma} \right]}, \tag{2.7}$$

$$M_i = \left[ (IPR^{(\gamma-1)/\gamma} - 1) \frac{2}{\gamma - 1} \right]^{0.5}. \tag{2.8}$$

### 2.3. Pressure measurement and flow visualization

The total pressure of the main jet is measured using a Pitot tube with inner and outer diameters of 0.6 and 0.9 mm, respectively, which is connected to a miniature pressure transducer (MEAS XPM4-5BA-/ET1) with a measurement range of 0–5 bar and linearity up to a maximum departure of 0.25%. During measurements, the Pitot probe induces a bow shock wave ahead of its head (figure 2). Therefore, the measured total pressure could be less than the actual total pressure due to the pressure loss associated with the shock wave. The total pressure loss is negligibly small since the shock strength is impaired as the Pitot probe is moved downstream and the flow upstream of the bow shock wave is virtually undisturbed (Katanoda *et al.* 2000). As such, no correction is made for the pressure measurement. Rathakrishnan (2016) advocated that, when the ratio of the nozzle exit area to the probe projected area is greater than 64, the probe interference to the flow is negligibly small. This view is reinforced by numerous investigations. Miller *et al.* (2009) compared the total pressure measured using a Pitot probe and that calculated from the Reynolds-averaged Navier–Stokes (RANS) simulation of  $M_j = 1.3$  and 1.5 jets. Their blockage ratio was 161. The two sets of data show excellent agreement (their figure 10) even at  $x^* = 0-2$ , where a strong shock occurred due to the presence of the Pitot probe (figure 2). Miller & Veltin (2011) compared the velocity profiles of an  $M_j = 1.5$  jet at various  $x^*$  (up to 8), measured from a rake of five Pitot probes, with that of the RANS simulation. Their blockage ratio was about 90. The comparison was very good (their figures 3 and 4), especially when the total temperature ratio was less than 3.6 (the present ratio is about 1). A similar observation was also made by André, Castelain & Bailly (2013) for  $M_j = 1.15$  and 1.5 jets where the Pitot-probe-measured velocities were compared with laser Doppler velocimetry data (their probe blockage ratio was 652). As a matter of fact, the Pitot probe

## A minijet-manipulated supersonic jet

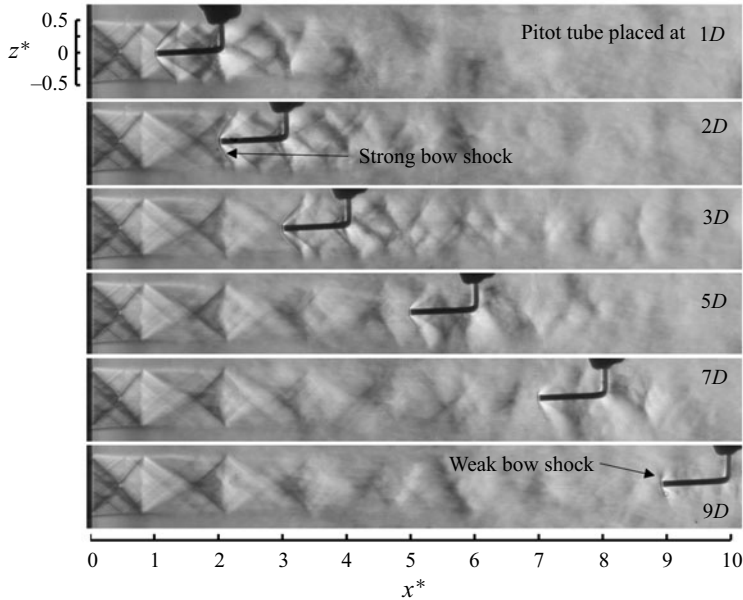


Figure 2. Schlieren images of supersonic natural jets,  $NPR = 4.0$  ( $P_e/P_a = 0.70$ ). Pitot tube at various  $x^*$  locations.

blockage effects are insignificant even when the probe blockage ratio is smaller than 64. For example, Katanoda *et al.* (2000) observed in an  $M_j = 2$  jet that the total pressure, measured using a Pitot probe with a blockage ratio of 42, agreed well with numerical simulation based on the Euler equation. Phalnikar, Kumar & Alvi (2008) showed that the shock-cell spacing measured using a Pitot probe with a blockage ratio of 16 was in excellent agreement with the estimate from shadowgraph images (their figures 7 and 8). The present probe blockage ratio is 123, and the probe interference to the flow should be negligibly small.

The Pitot tube is traversed within the range of  $(x^*, y^*, z^*) = (0-20, -2-2, -2-2)$ . As noted by Perumal & Rathakrishnan (2022), the measured pressure  $P_{0t}$  can be used to determine  $L_c^*$ , which is currently used to quantify jet mixing. The  $Re$  based on the inner diameter of the Pitot tube is  $10^4$ , well above 200, and therefore the viscous effect on the measured total pressure can be safely neglected (Chue 1975). The raw data are recorded at a sampling frequency of 2000 Hz for a duration of 2 s by a PC through a 16-bit National Instruments DAQ board (6361) and then fed into LabVIEW for data processing.

A conventional Z-type schlieren system is used for flow visualization (figure 1b). Two concave mirrors, each with a diameter of 200 mm and a focal length of 2000 mm, have a surface finish of  $\lambda/10$ , where  $\lambda$  denotes the light wavelength. Illumination is provided by a white-light source that passes through two condenser lenses before reaching one of the concave mirrors. A parallel beam from the first mirror passes through the test section before being projected on another mirror and is then focused on a knife edge before being projected on a screen. The time-averaged and instantaneous images are recorded at a sampling frequency of 300–1000 Hz with an exposure of 1000  $\mu\text{s}$  and 30–90 kHz with an exposure of 1–3  $\mu\text{s}$ , respectively, using a Dantec camera ( $2560 \times 1600$  pixels), and then processed using PCC 2.12 software.

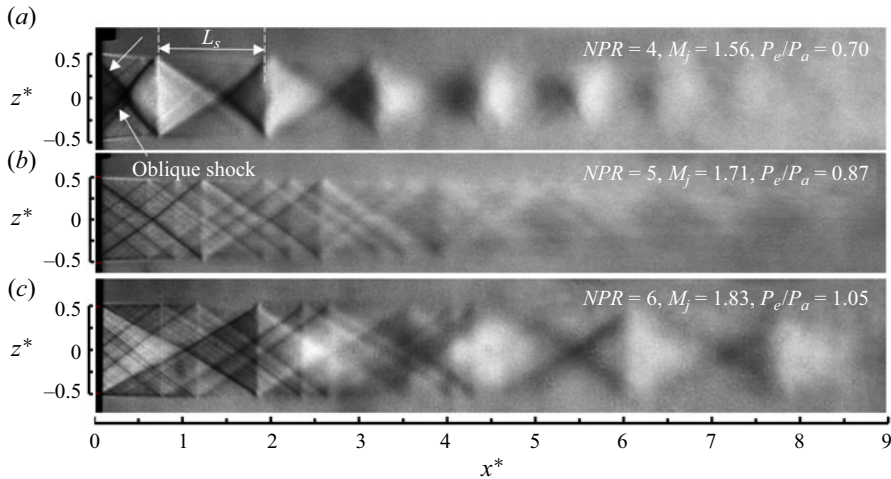


Figure 3. (a–c) Time-averaged schlieren images for various fully expanded jets with Mach number  $M_j$ . Parameter  $L_s$  is the shock-cell length.

### 3. Natural jet

The schlieren images of the natural jet at  $NPR = 4$ – $6$  (figure 3) display the familiar periodic shock-cell structure for a supersonic jet (e.g. Munday *et al.* 2011; Perumal *et al.* 2019). At  $NPR = 4$  ( $P_e/P_a = 0.70$ ,  $M_j = 1.56$ ), the jet is over-expanded, and two oblique shock waves are formed at the lip of the nozzle exit, as marked with arrows in figure 3(a), which act to increase the nozzle exit pressure to ambient pressure. The oblique shock waves intersect at the jet axis and cross each other, resulting in either a regular reflection or Mach reflection that depends on the magnitude of  $P_e/P_a$  (Zhang *et al.* 2019). In the present case, a regular reflection is observed. Further, the oblique shock waves downstream of the regular reflection reflect as Prandtl–Meyer expansion fans from the jet boundary. These fans are further reflected as shock waves from the jet boundary and cross each other at the jet axis or the so-called crossover point. This cycle continues until the flow finally reaches the subsonic state. A similar flow structure is also observed at  $NPR = 5$  and  $6$ .

The variation in  $P_{0t}/P_{0s}$  along the jet centreline for  $NPR = 4$ – $6$  is compared in figure 4 with that reported by Phanindra & Rathakrishnan (2010) at the same  $M_d$  and  $NPR$ . The two measurements agree well qualitatively despite an appreciable departure which is ascribed to a difference in the nozzle geometry between the two studies. As shown in the inset of figure 4(a), the divergent section is a straight line with a semi-divergent angle of  $7^\circ$  in Phanindra & Rathakrishnan (2010) but not in the present case. It is well known that a jet issuing from a straight nozzle is characterized by stronger shock/expansion waves (Cuppoletti *et al.* 2014). This is indeed confirmed in the present case. As indicated by the lower trough of  $P_{0t}/P_{0s}$ , their shock wave is stronger than the present one.

Length  $L_c$  is defined as the longitudinal distance from the nozzle exit to where  $M$  reaches unity, which scales with the mass entrainment of ambient fluid into the jet stream (Zaman, Reeder & Samimy 1994). Perumal & Rathakrishnan (2022) demonstrated a correlation between  $L_c$  and jet mixing. We may estimate  $L_c$  from the measured  $P_{0t}/P_{0s}$  data along the centreline (Khan *et al.* 2022; Perumal & Rathakrishnan 2022). For example, the cutoff



*A minijet-manipulated supersonic jet*

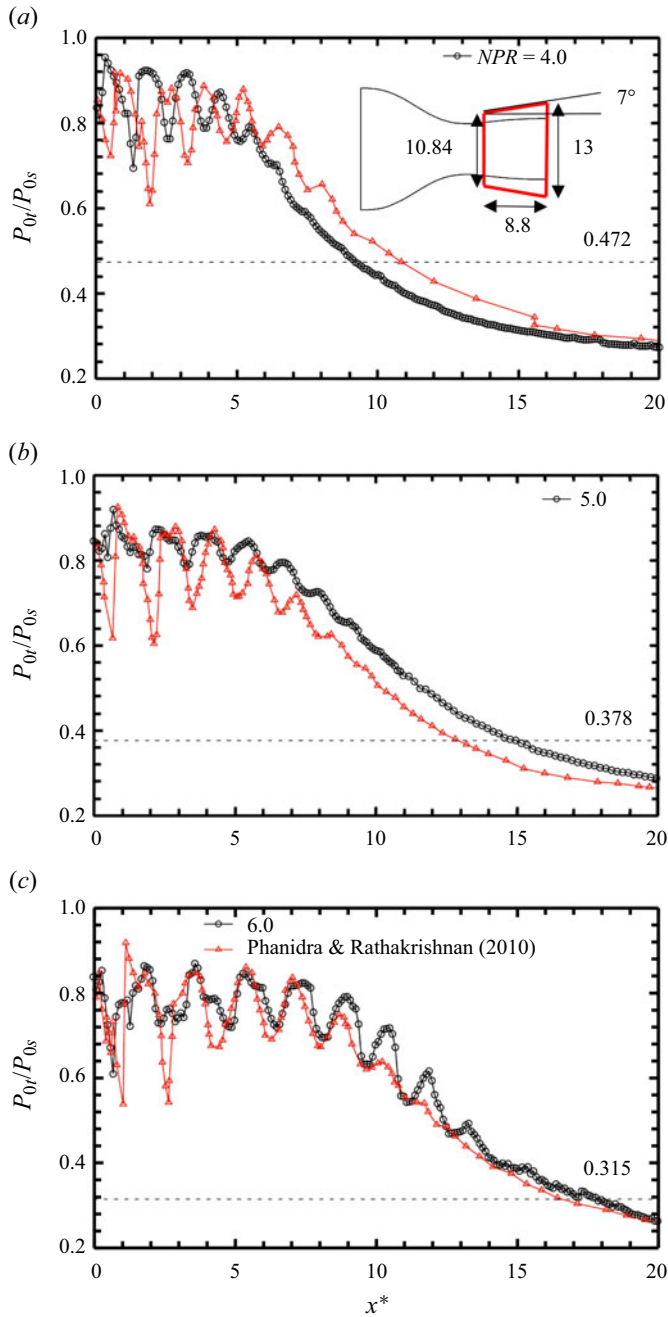


Figure 4. Time-averaged centreline pressure ratio at NPR of (a) 4, (b) 5 and (c) 6. The data of Phanindra & Rathakrishnan (2010), whose nozzle is given in red in the inset of (a), from an  $M_d = 1.8$  jet with the same NPR are included for comparison. The horizontal broken line indicates the cutoff  $P_{0t}/P_{0s}$  for sonic Mach number as given by Perumal & Rathakrishnan (2022).

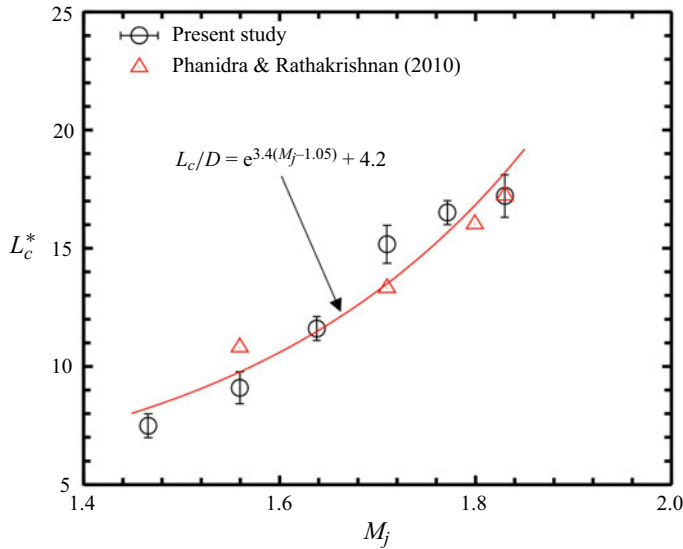


Figure 5. Variation with fully expanded jet Mach number  $M_j$  in the supersonic core length  $L_c^*$ . The data from Phanindra & Rathakrishnan (2010) for design Mach number  $M_d = 1.8$  are included for comparison. The curve is a least-squares fitting to experimental data.

ratio  $P_{0t}/P_{0s}$  for  $M = 1$  is given by the ratio of 1.89 (Anderson 1982) to the operating  $NPR$ :

$$\left(\frac{P_{0t}}{P_{0s}}\right)_{M=1} = \frac{P_{0t}/P_a}{P_{0s}/P_a} = \frac{1.89}{NPR}. \quad (3.1)$$

For  $NPR = 4$  or  $M_j = 1.56$ , the cutoff  $P_{0t}/P_{0s}$  is  $1.89/4 = 0.472$ , and the present  $L_c^*$  and that of Phanindra & Rathakrishnan (2010) are 9.1 and 10.7, respectively, with a deviation of 18 % (figure 5), which diminishes for higher  $M_j$ : 12.6 % and 3.5 % for  $M_j = 1.71$  and 1.83, respectively. This deviation is not unexpected in view of the difference in the measured  $P_{0t}/P_{0s}$  between the two studies (figure 4). The relationship between  $L_c^*$  and  $M_j$  can be obtained using the least squares fitting to the data:

$$L_c^* = e^{3.4(M_j-1.05)} + 4.2. \quad (3.2)$$

Jet spread in the radial direction is illustrated by the variation in the distribution of  $P_{0t}/P_{0s}$  ( $NPR = 4$ ) against  $z^*$  or  $y^*$  from  $x^* = 1$  to 20 (figure 6), which appears to be axisymmetric. At  $x^* = 1$ ,  $P_{0t}/P_{0s}$  exhibits a flat-top-hat distribution, implying a uniform Mach number around the jet axis. This is then followed by a steep decrease over  $-0.4 > y^* > 0.4$  and  $-0.4 > z^* > 0.4$  due to rapid mixing. For  $x^* = 7$  and 11,  $P_{0t}/P_{0s}$  exhibits a rapid drop in its centreline value and a radial growth. The jet appears fully developed at  $x^* = 20$ , as noted by Phanindra & Rathakrishnan (2010).

#### 4. Jet mixing of manipulated jet

##### 4.1. Effects of the control parameters on jet mixing

It is well known that a jet manipulated using a single minijet may deflect, referred to as thrust vectoring. As a result, jet mixing quantified based on a change in the centreline velocity or pressure may be artificially exaggerated. Following Perumal & Rathakrishnan

A minijet-manipulated supersonic jet

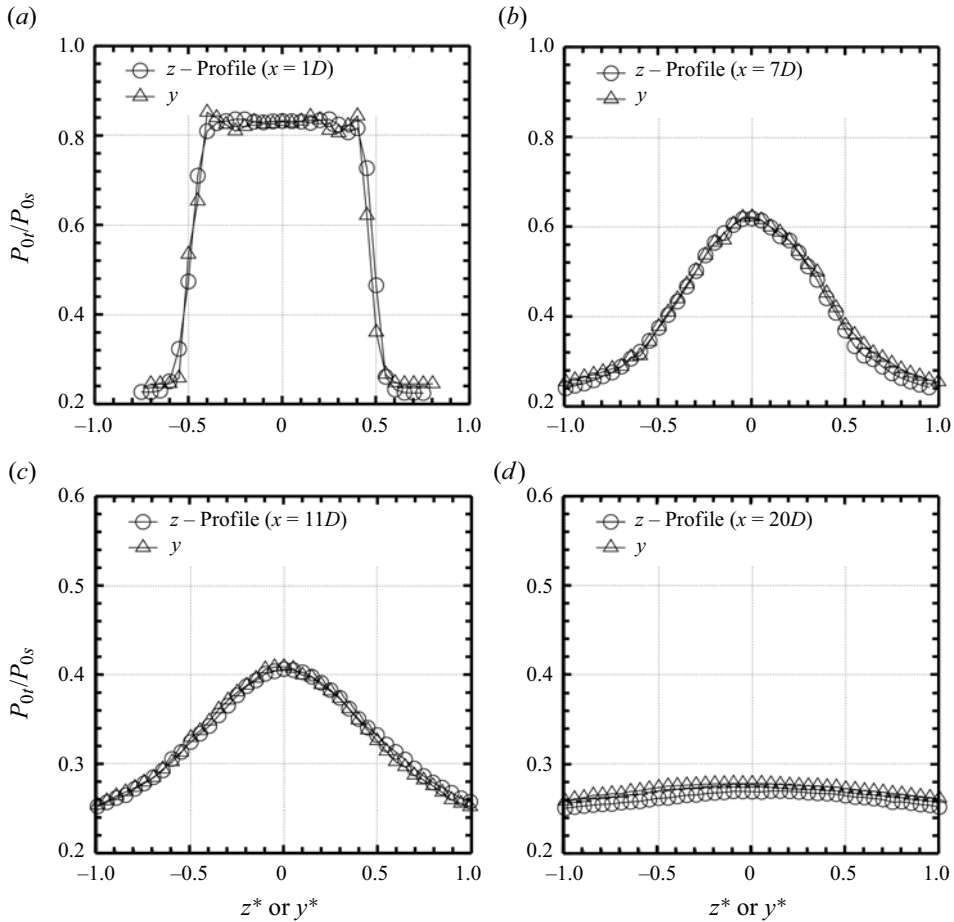


Figure 6. (a–d) Radial pressure ratio distributions of natural jet at exit pressure ratio  $P_e/P_a = 0.70$ .

(2021), we may estimate  $L_c^*$  from the actual position of the measured maximum  $P_{0t}/P_{0s}$ . Note that the minijet injection is along the positive  $z$  direction. Figure 7 presents the contours of time-averaged  $P_{0t}/P_{0s}$  measured in the injection and non-injection planes or  $xz$  and  $xy$  planes for various  $C_m$  ( $d/D = 1/9.5$ ,  $P_e/P_a = 0.70$ ) along with those of the natural jet ( $P_e/P_a = 0.70$ ). The contours are symmetric about the centreline ( $y^* = z^* = 0$ ) for the natural jet (figure 7a) but asymmetric in the  $xz$  plane under manipulation (figure 7b–d), where the maximum  $P_{0t}/P_{0s}$  occurs at a negative  $z^*$ , suggesting a deflected jet. This deflection becomes more obvious with increasing  $C_m$ . In the  $xy$  plane, the contours show slight asymmetry about  $y^* = 0$  (figure 7e–g). Therefore, we determine  $L_c^*$  directly from the  $P_{0t}/P_{0s}$  contours based on the cutoff level of  $M = 1$  (Anderson 1982) (figure 7a–g). Note that the estimated  $L_c^*$  in the  $xy$  plane (figure 7e–g) is shorter than in the  $xz$  plane (figure 7b–d). This observation is internally consistent with the fact that the  $xy$  plane cuts through the  $xz$  plane where the sonic Mach number is not a maximum. Similar observations are also made at other  $P_e/P_a$ .

There are two factors that may contribute to the asymmetry of the pressure contours about  $y^* = 0$  in the  $xy$  plane. One is ascribed to experimental uncertainties, which could be eliminated if the sample size is infinitely large. The present sampling rate and duration

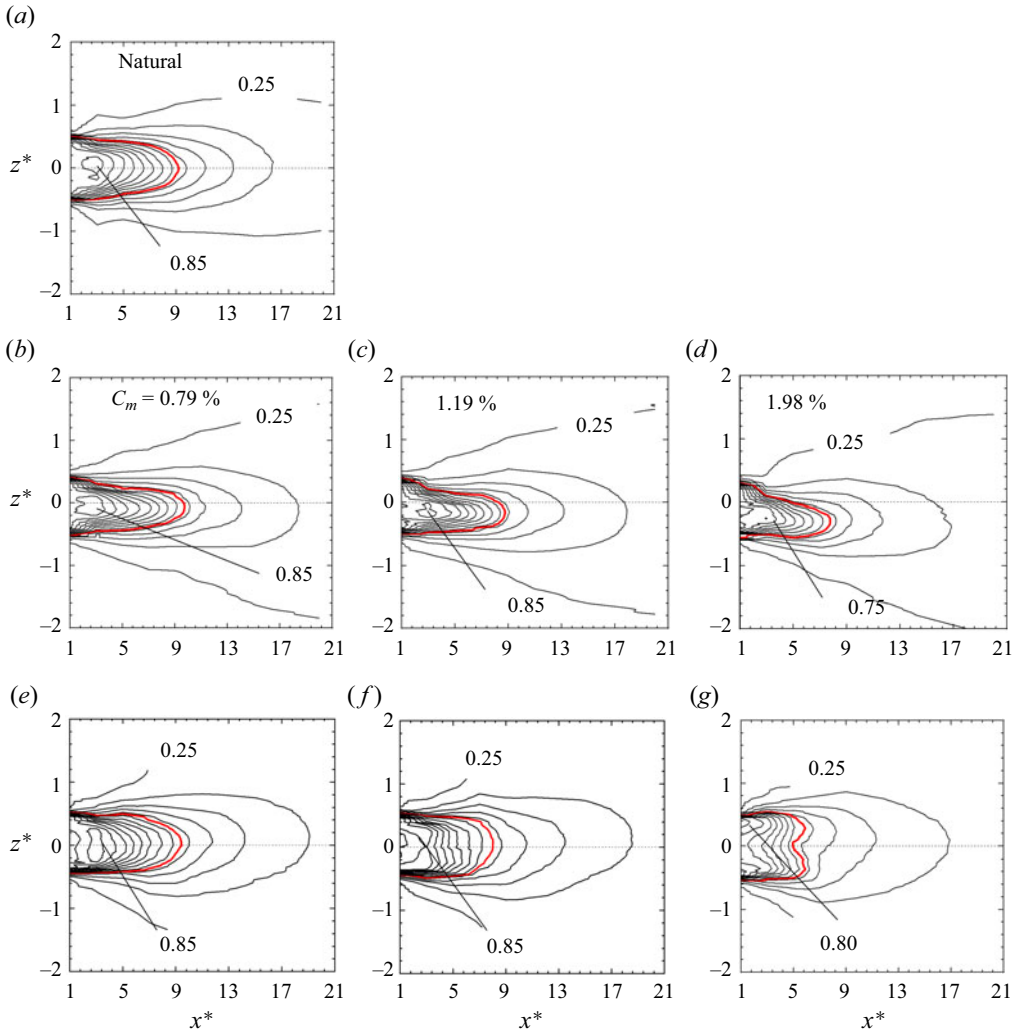


Figure 7. Iso-contours of time-averaged pressure ratio  $P_{0t}/P_{0s}$ . (a) Natural jet ( $P_e/P_a = 0.70$ ). Manipulated jet ( $d/D = 1/9.5$ ): (b–d) injection plane; (e–g) non-injection plane. The red thick curve denotes the cutoff pressure ratio (0.472) for the sonic Mach number.

of the pressure data were limited, 2000 Hz and 2 s, respectively. The choice of the 2 s sampling duration is based on a convergence test. The variation in the pressure data obtained at  $(x^*, y^*, z^*) = (0.5, 0, 0)$  of the natural jet ( $NPR = 4$ ) is converged to within 1% once the sampling duration exceeds 1.8 s (not shown). Another factor could be linked to the part of the L-shape Pitot tube (figure 2), which is normal to the flow and located downstream of the pressure data obtained. When the Pitot tube is traversed across the jet, this part may interfere with the pressure data obtained upstream at  $y^* = -1.5-0$ . This interference retreats at  $y^* = 0-1.5$ , where the blockage produced by the Pitot tube is smaller. Note that the jet asymmetry is appreciable only downstream of the cutoff pressure (see the red-coloured contour in figure 7e–g) that is used to estimate  $L_c^*$ . That is, the jet asymmetry takes place downstream of the supersonic potential core, where the flow is subsonic, thus being more susceptible to downstream disturbance. It is worth pointing out

## A minijet-manipulated supersonic jet

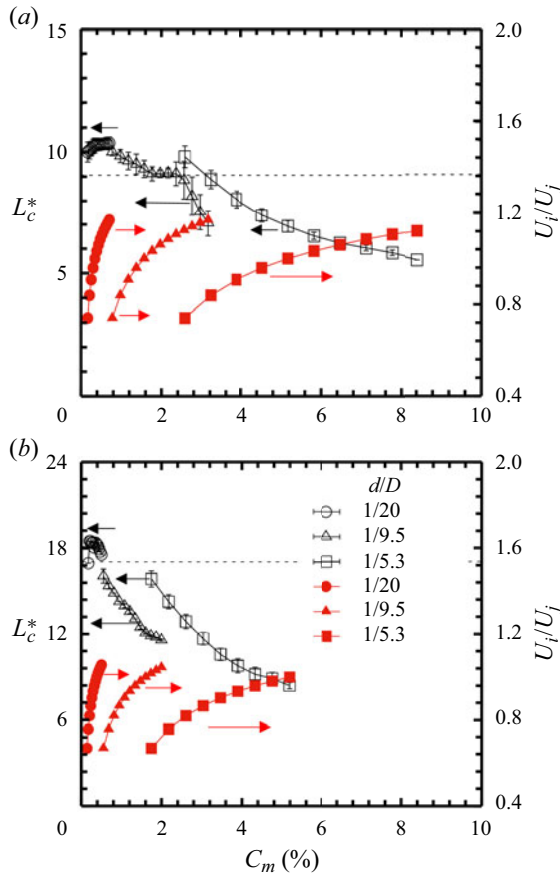


Figure 8. Dependence of the supersonic core length  $L_c^*$  on mass flow rate ratio  $C_m$  and correlation between velocity ratio  $U_i/U_j$  and  $C_m$ : (a)  $P_e/P_a = 0.70$ , (b) 1.05. The dotted line represents  $L_c^*$  of natural jet.

that this asymmetry of the pressure data in the  $xy$  plane produces essentially no effect on the estimate of  $L_c^*$ , which is determined only from the pressure data measured in the  $xz$  plane as described before.

One can see a pressure dip at  $y^* = 0$  in figure 7(g) for  $C_m \geq 1.98\%$  at  $(P_e/P_a, d/D) = (0.70, 1/9.5)$  when the  $IPR$  is quite large ( $= 5$ ). This is because at very large  $C_m$  or  $IPR$ , the penetration depth of the minijet is also large, causing the cross-section of the main jet to deform into a kidney-shaped structure, as observed by Zaman *et al.* (1994) in a supersonic jet manipulated by a single tab. Note that the injection is along the positive  $z^*$  direction. This kidney-shaped structure produces a double peak in the pressure profile, thus causing the dip at  $y^* = 0$  in the  $xy$  plane.

Figure 8 presents the variation in  $L_c^*$  with  $C_m$  for  $d/D = 1/20$ – $1/5.3$  and  $P_e/P_a = 0.70$  and 1.05. The control is considered to be effective once  $L_c^*$  falls below that of the natural jet ( $C_m = 0$ ). Several observations can be made. First, for  $d/D \geq 1/9.5$ ,  $L_c^*$  retreats with increasing  $C_m$ , regardless of  $P_e/P_a$ . At  $P_e/P_a = 0.70$ ,  $L_c^*$  is larger than that of the natural jet for  $C_m < 1.8\%$  but smaller for  $C_m \geq 1.8\%$ . The minijet injection at small  $C_m$  is unable to penetrate the main jet core (figure 7b–d) and may be swept away downstream (Davis 1982). In their manipulation of an  $M_d = 1.1$  jet using 16 minijets at  $d/D = 1/33$  ( $C_m = 0.9\%$ ), Callender, Gutmark & Martens (2007) also observed an increased jet core length with respect to the natural jet. They argued, based on particle image velocimetry data, that the

minijets acted as a shield for the main jet and impeded the shear-layer growth, resulting in a prolonged jet core. On the other hand, the minijet injection penetrates the main jet core given a larger  $C_m$ , resulting in a reduced  $L_c^*$ . Second, for  $d/D = 1/20$ ,  $L_c^*$  increases with increasing  $C_m$  until reaching a local maximum, which may vary with  $P_e/P_a$ , and then drops with a further increase in  $C_m$ . The value of  $L_c^*$  exceeds that of the natural jet for the range of  $C_m$  examined. The present  $P_{0i}/P_{0s}$  contours (not shown) of the manipulated jet for  $d/D = 1/20$  do not show any sign of minijet penetration into the shear layer of the main jet. Third, for a given  $C_m$ , an increase in  $d/D$  leads to a significant increase in  $L_c^*$ , suggesting that small  $d/D$  promotes jet mixing, though  $d/D$  cannot be too small, say below  $1/20$  in the present case. Evidently, a smaller  $d/D$  for a given  $C_m$  leads to a higher  $U_i/U_j$ , and hence deeper penetration into the main jet. Finally, given  $d/D$  and  $C_m$ , the manipulated jet at  $P_e/P_a = 1.05$  experiences a more significant contraction in  $L_c^*$  than at  $P_e/P_a = 0.70$ . For example, given  $d/D = 1/5.3$  and  $C_m = 3.2\%$ ,  $L_c^*$  drops from 17.1 without control to 10.6 at  $P_e/P_a = 1.05$ , a decrease of 38%. At  $P_e/P_a = 0.70$ , however,  $L_c^*$  reduces by only 22% for the same  $d/D$  and  $C_m$ . This suggests a more effective manipulation under the design condition ( $P_e/P_a = 1$ ) than under off-design conditions ( $P_e/P_a \neq 1$ ). In their manipulation of a  $NPR_d = 4$  ( $M_d = 1.56$ ) jet at  $NPR = 2.5\text{--}4.5$  using 24 minijets, Cuppoletti & Gutmark (2014) reported a more pronounced noise reduction at  $NPR_d = 4$  than at other  $NPR$  values. Their particle image velocimetry measurements showed that the strength of normalized streamwise vortices and shear-layer thickness under the design condition exceeded those of the off-design condition due to deeper penetration, even though the design condition corresponded to smaller  $C_m$ . It may be inferred that the perfectly expanded jet ( $P_e/P_a = 1.05$ ) may experience a deeper minijet penetration into the main jet, thus weakening the shock cells more substantially, than under the off-design condition ( $P_e/P_a = 0.70$ ).

#### 4.2. Scaling law of control

As discussed in § 4.1,  $L_c^*$  depends strongly on  $C_m$ ,  $d/D$  and  $P_e/P_a$ , and jet mixing is correlated with the penetration depth of the minijet into the main jet (Perumal & Zhou 2018). The ratios  $U_i/U_j$  and  $d/D$  are related via  $C_m$ , where  $U_j$  and  $U_i$  are calculated from (2.3) and (2.7), respectively (figure 8). Apparently, for a given  $C_m$ ,  $U_i/U_j$  increases with decreasing  $d/D$ , which is consistent with our earlier discussion that jet mixing is enhanced as  $d/D$  reduces. Further,  $C_m$  required to achieve the same  $U_i/U_j$  drops given a smaller  $d/D$ . Note that either  $U_i/U_j$  or  $C_m$  may affect directly the penetration depth (Davis 1982; Semlitsch *et al.* 2019) that scales with  $MR_N$  (Henderson 2010). Khan *et al.* (2022) and Perumal & Rathakrishnan (2022) performed empirical scaling analysis based on experimental data of jets of  $M_d = 1.5$  and 2.0, manipulated using  $N$  ( $= 2\text{--}6$ ) minijets, and found indeed that jet mixing scales with the square root of  $MR_N$  ( $= C_{m,N} U_i/U_j$ ), where  $C_{m,N}$  is the mass flow rate ratio of an individual minijet to the main jet. Their scaling law involves only a fixed  $d/D$ . Then one question arises: can we find a scaling law that incorporates varying  $d/D$ ?

Let us consider  $L_c^* = f_1(C_m, d/D, P_e/P_a, M_j)$ . A supersonic jet is characterized by  $P_e/P_a$  and  $M_j$  (Driftmyer 1972). Thus, a developed scaling law with both  $P_e/P_a$  and  $M_j$  incorporated may be applied for varying  $M_d$  (Werle, Shaffer & Driftmyer 1970). To further accommodate different gas species, we may include  $\gamma$  in the scaling law to be developed. Then we have  $L_c^* = f_2(C_m, d/D, P_e/P_a, M_j, \gamma)$ . Tam, Seiner & Yu (1986) introduced a new parameter  $D_j$ , i.e. the fully expanded diameter, accounting for the jet contracting and expanding at the nozzle exit due to off-design conditions, and  $D_j$  is related to  $D$  through

mass conservation:

$$\frac{D_j}{D} = \left[ \frac{1 + \frac{1}{2}(\gamma - 1)M_j^2}{1 + \frac{1}{2}(\gamma - 1)M_d^2} \right]^{(\gamma+1)/4(\gamma-1)} \left( \frac{M_d}{M_j} \right)^{1/2}. \quad (4.1)$$

Under the design condition,  $M_j = M_d$ , implying  $D_j = D$ ; under the off-design condition,  $M_j \neq M_d$  and  $D_j \neq D$ . Similarly, we may introduce the fully expanded diameter  $d_i$  for the minijet:

$$\frac{d_i}{d} = \left[ \frac{1 + \frac{1}{2}(\gamma - 1)M_i^2}{1 + \frac{1}{2}(\gamma - 1)} \right]^{(\gamma+1)/4(\gamma-1)} \left( \frac{1}{M_i} \right)^{1/2}, \quad (4.2)$$

where  $M_d$  is 1 since the nozzle of the minijet is a simple constant-diameter tube. As such, we have  $L_c^* = f_3(C_m, d_i/D_j, P_e/P_a, M_j, \gamma)$ , which accounts for the contracting and expanding of both minijet and main jet.

Since  $C_m$  is related to  $d/D$ ,  $d_i/D_j$  is implicitly included in  $C_m$ . To explicitly retain  $d_i/D_j$ , following Muppidi & Mahesh (2005) one may rewrite  $L_c^* = f_3(C_m, d_i/D_j, P_e/P_a, M_j, \gamma)$  as  $L_c^* = f_4(J, d_i/D_j, P_e/P_a, M_j, \gamma)$ , where  $J = \sqrt{\rho_i U_i^2 / (\rho_j U_j^2)}$  is the momentum flux ratio of the minijet to the main jet,  $\rho_i$  and  $\rho_j$  are calculated from (4.3) and (2.4), respectively, and  $U_i/U_j$  is implicitly included in  $C_m$ :

$$\rho_i = \left( \frac{IPR \times P_a}{RT_0} \right) / \left( 1 + \frac{\gamma - 1}{2} M_i^2 \right)^{1/(\gamma-1)}. \quad (4.3)$$

Following Werle et al. (1970), we may further simplify  $L_c^* = f_4(J, d_i/D_j, P_e/P_a, M_j, \gamma)$  as  $L_c^* = f_5(Jd_i/D_j, \gamma M_j^2 P_e/P_a)$ , where  $\gamma M_j^2 P_e/P_a$  is a standard dimensionless pressure ratio in compressible flow theory and in the present case is the non-dimensional exit pressure ratio. Those authors and also Driftmyer (1972) developed a scaling law to predict the terminal shock position  $h$  with respect to the nozzle exit of a highly under-expanded jet and postulated that  $h/b_e$  scales with  $\gamma M_j^2 P_e/P_a$ , where  $b_e$  is the width of the nozzle exit. Then following Perumal & Rathakrishnan (2022), we may rewrite  $L_c^* = f_5(Jd_i/D_j, \gamma M_j^2 P_e/P_a)$  as

$$L_c^* \propto \frac{Jd_i/D_j}{\gamma M_j^2 P_e/P_a}. \quad (4.4)$$

As a matter of fact, the data in figure 8 collapse reasonably well provided  $(Jd_i/D_j)/(\gamma M_j^2 P_e/P_a)$  is used as the abscissa (figure 9), which may be least-squares-fitted to

$$L_c^* = 20.9 e^{-34\xi} + 5.1. \quad (4.5)$$

That is,  $L_c^* = f_2(C_m, d/D, P_e/P_a, M_j, \gamma)$  may be reduced to  $L_c^* = f_6(\xi)$ , where the scaling factor  $\xi = (Jd_i/D_j)/(\gamma M_j^2 P_e/P_a)$ . The data above the horizontal dashed line in figure 8 are not included in figure 9 since the scaling law is developed for jet mixing enhancement.

Several points can be made from the scaling equation (4.5). Firstly, to our surprise, Perumal & Rathakrishnan's (2022) data from a jet of  $M_d = 2.0$  manipulated with two oppositely placed minijets also collapse reasonably well about the scaling law (not shown). Since the two investigations differ in  $M_d$  as well as  $N$ , it seems plausible that the scaling law is valid for varying  $M_d$ . Secondly, Perumal & Rathakrishnan (2022) found that  $L_c^*$

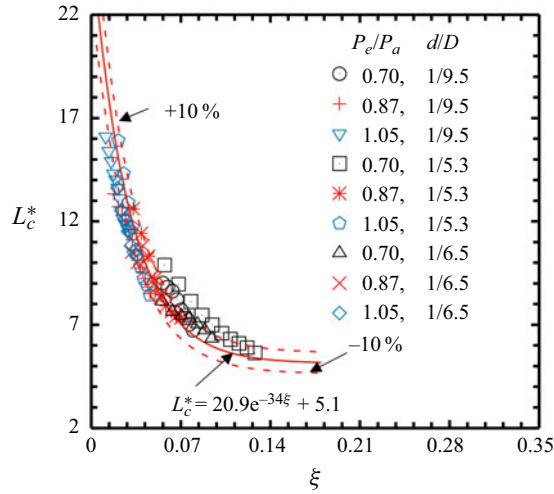


Figure 9. Dependence of the supersonic core length  $L_c^*$  on the scaling factor  $\xi = \sqrt{C_m U_i / U_j} / (\gamma M_j^2 P_e / P_a) = J(d_i / D_j) / (\gamma M_j^2 P_e / P_a)$ , where the momentum flux ratio  $J = \sqrt{\rho_i U_i^2 / (\rho_j U_j^2)}$ . The solid curve is the least-squares fitting to experimental data and the broken curves indicate the confidence levels of +10% and -10%.

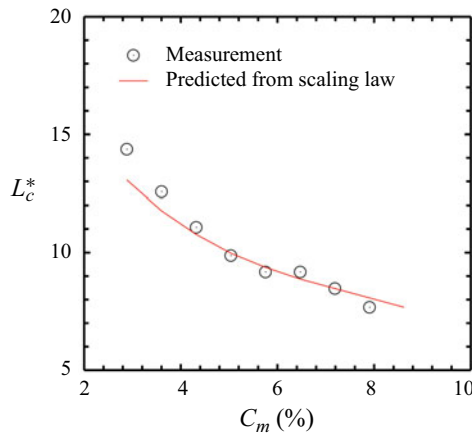


Figure 10. Dependence of predicted supersonic core length  $L_c^*$  on mass flow rate ratio  $C_m$  from the scaling law (4.5) ( $P_e/P_a = 1.05$ ,  $d/D = 4.1$ ), as compared with measured  $L_c^*$  under identical conditions.

scales with  $\sqrt{MR_N} / (\gamma M_j^2 P_e / P_a)$ , implying an analogy between  $(Jd_i / D_j) / (\gamma M_j^2 P_e / P_a)$  and  $\sqrt{MR_N} / (\gamma M_j^2 P_e / P_a)$  due to  $Jd_i / D_j = \sqrt{MR_N}$ . Apparently, the present scaling law includes one additional parameter  $d_i / D_j$ . It may be inferred that  $Jd_i / D_j$  is the square root of the momentum ratio of minijet to main jet. Lastly, in order to confirm the robustness of the scaling law, we have performed additional experiments for  $d/D = 1/4.1$  and  $C_m = 2.88\% - 7.91\%$  ( $M_j = 1.56$ ,  $P_e/P_a = 0.70$ ). Figure 10 shows that the data obtained at  $d/D = 1/4.1$  agree reasonably well with the prediction from scaling law (4.5) for the same  $C_m$ ,  $d/D$  and  $P_e/P_a$ . Similar observation has also been made for other  $P_e/P_a$ . The results suggest the robustness of the scaling law.



### A minijet-manipulated supersonic jet

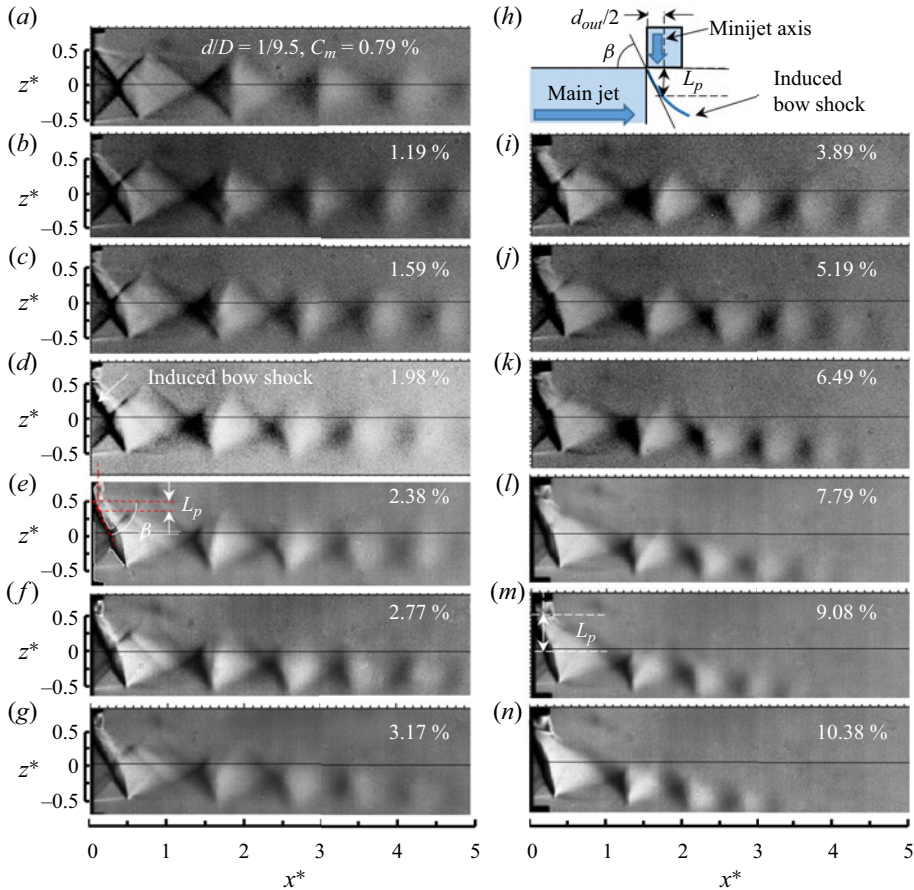


Figure 11. (a–g,i–n) Time-averaged schlieren images of manipulated jet at  $P_e/P_a = 0.70$  for various  $C_m$  along with (e,h) the definitions of the shock wave angle  $\beta$  and the distance  $L_p$  from the nozzle lip ( $z^* = 0.5$ ) to the point where the induced bow shock and the minijet centreline intersect.

#### 4.3. Interesting aspects of the scaling law

An attempt is made to understand the physical meaning of  $\xi$ . Perumal & Zhou (2018, 2021) quantified the penetration depth of the minijet into the main jet based on the root-mean-square values of the streamwise velocity at the nozzle exit and observed a strong correlation between the penetration depth and  $C_m$ . This depth has never been quantified in the context of a supersonic jet. As shown in figure 11, the minijet injection induces a bow shock. The bow shock angle  $\beta$  with respect to the streamwise direction and the distance  $L_p$  between the nozzle lip ( $z^* = 0.5$ ) and the intersection point of the bow shock and minijet centreline, as defined in figure 11(h), are apparently correlated with  $C_m$ . An increase in  $C_m$  is associated with an increase in  $\beta$  and also  $L_p$ . It seems plausible that either  $L_p$  or  $\beta$  may provide a measure for the minijet penetration into the main jet. Figure 12 presents the dependences of  $L_c^*$  and  $\xi$  on  $L_p^*$  and  $\beta$ , respectively, for various  $C_m$ ,  $P_e/P_a$  and  $d/D$ . Obviously,  $L_c^*$  decreases with increasing  $L_p^*$  and  $\beta$ , corresponding to enhanced jet mixing. Furthermore,  $\xi$  is positively correlated with  $L_p^*$  and  $\beta$ . The results suggest that the scaling factor  $\xi$  may be physically interpreted as the penetration depth of the minijet into the main jet, which may determine the level of jet mixing measured through  $L_c^*$ .

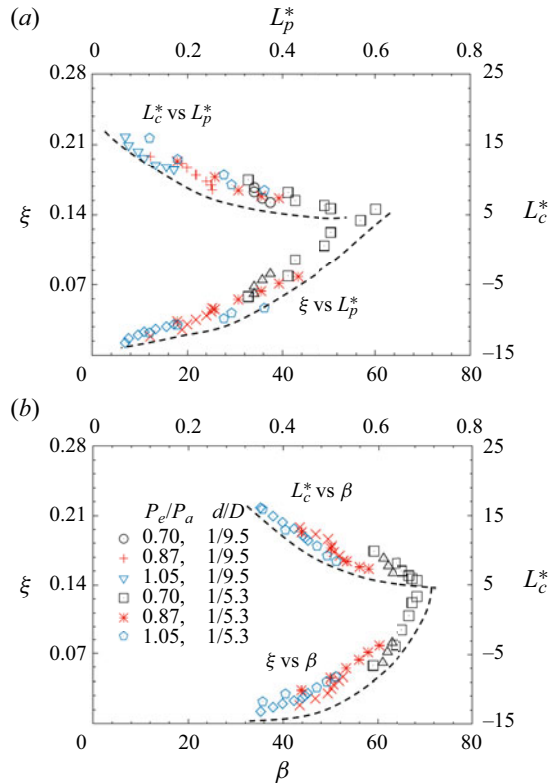


Figure 12. Dependence of the scaling factor  $\xi$  and supersonic core length  $L_c^*$  on (a) the penetration depth  $L_p^*$  and (b) shock wave angle  $\beta$ .

One of the important applications of the scaling law is to predict the optimal  $d/D$  at which the required jet mixing is achieved with a minimal consumption of  $C_m$  and  $IPR < NPR$ . In practice, there are two factors to be considered when we employ minijets for jet manipulation. One is to have an  $IPR$  less than the operating  $NPR$ . The other is to make  $C_m$  as small as possible, achieving the desired performance with the minimum consumption of injection mass flow rate. It is not uncommon to bleed a maximum of 5% of air flow entering an engine for the purpose of minijet injection as the bleed is associated with an engine thrust loss (Smith, Cain & Chenault 2001).

As noted earlier, jet mixing benefits from small  $d/D$ , at which the required  $C_m$  is small in achieving a given  $L_c^*$  as long as  $d/D > 1/20$ . For example, to achieve a predefined  $L_c^* = 8.0$  at  $P_e/P_a = 0.70$  ( $NPR = 4$ ), the required  $C_m$  and  $IPR$  for  $d/D = 1/9.5$  are 3% (figure 8) and 7.5 (table 2), respectively. In this case,  $IPR > NPR$ . When  $d/D$  is increased to 1/5.3, the  $IPR$  drops to 3.25 (table 2) so that  $IPR < NPR$ , whereas the required  $C_m$  increases to 4% (figure 8). The result suggests the presence of an optimal  $d/D$  at which  $IPR < NPR$  and  $C_m \leq 5\%$ . The optimal  $d/D$  may be predicted based on the scaling law for a given  $M_j$ . Assume  $IPR = NPR$  and the predefined  $\Delta L_c^* = 15\%$  and  $25\%$ , where  $\Delta L_c^*$  is the desired jet mixing enhancement defined by

$$\Delta L_c^* = \frac{(L_c^*)_{natural} - (L_c^*)_{manipulated}}{(L_c^*)_{natural}} \times 100. \quad (4.6)$$

### A minijet-manipulated supersonic jet

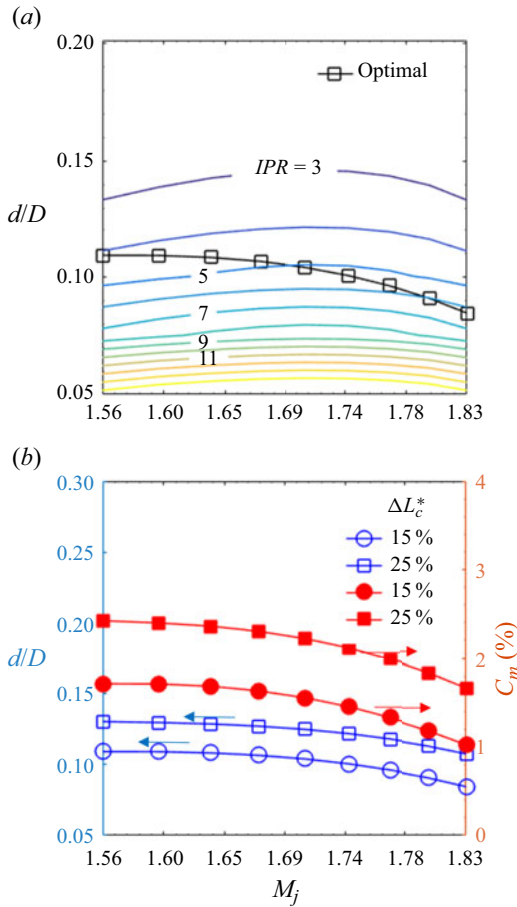


Figure 13. (a) Dependence of  $IPR$  on diameter ratio  $d/D$  and fully expanded jet Mach number  $M_j$  ( $\Delta L_c^* = 15\%$ ), where the square symbols correspond to  $d/D$  at which  $IPR = NPR$  ( $IPR < NPR$  and  $IPR > NPR$  occur above and below the symbols, respectively). (b) Dependence of  $C_m$  and  $d/D$  on  $M_j$ .

In (4.6), subscripts ‘manipulated’ and ‘natural’ denote the manipulated and natural jets, respectively. To predict the optimal  $d/D$ , we first determine the required  $(L_c^*)_{manipulated}$  for given  $\Delta L_c^*$  and  $M_j$  from (3.2) and (4.6) and then calculate  $d/D$  from (4.1)–(4.5). The obtained optimal  $d/D$  is presented in figure 13(a), from which several observations can be made. The optimal  $d/D$  decreases with increasing  $M_j$ , which is not feasible for practical applications. To avoid this, we may choose the optimal  $d/D$  based on the minimum operating  $M_j$ . If the choice of the optimal  $d/D$  is based on the maximum operating  $M_j$ , then the required  $IPR$  at the other operating  $M_j$  would exceed  $NPR$ . For example, if the optimal  $d/D = 0.08$  is chosen based on  $M_j = 1.83$ , then for  $M_j = 1.69$  ( $NPR = 4.9$ ) the required  $IPR$  is about 7 (figure 13a), greater than the operating  $NPR = 4.9$ . On the other hand, the required  $IPR$  at the other operating  $M_j$  will be less than  $NPR$  provided the optimal  $d/D$  is determined from the minimum operating  $M_j$ .

With the optimal  $d/D$  known, we may calculate the required  $C_m$  from (2.5)–(2.6). As shown in figure 13(b), the required  $C_m$  drops with increasing  $M_j$  and reaches the minimum at the design Mach number, suggesting an efficient jet manipulation, which is internally consistent with the observation from figure 8. Obviously, the choice of the optimal  $d/D$

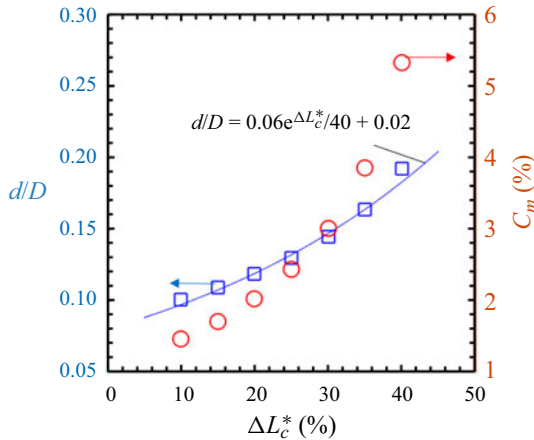


Figure 14. Dependence of the optimal  $d/D$  and  $C_m$  on  $\Delta L_c^*$  at  $M_j = 1.56$ . The curve is the least-squares fitting to the optimal diameter ratios.

depends on the minimum operating  $M_j$  as well as available  $C_m$ . One may also wonder how the optimal  $d/D$  would vary if  $\Delta L_c^* = 15\%$  increases to  $25\%$ . As shown in figure 13(b), the optimal  $d/D$  becomes in general larger at  $\Delta L_c^* = 25\%$  than at  $15\%$ . For example, at  $M_j = 1.56$ , the optimal  $d/D$  is 0.11 for  $\Delta L_c^* = 15\%$  and 0.13 for  $\Delta L_c^* = 25\%$ . Further, the optimal  $d/D$  may increase with increasing  $\Delta L_c^*$ , as is evident in figure 14 ( $M_j = 1.56$ ). The required  $C_m$  exceeds  $5\%$  once  $\Delta L_c^* > 40\%$ . Therefore, it can be inferred from the above discussion that the optimal  $d/D$  is a trade-off between  $\Delta L_c^*$ , the minimum operating  $M_j$  or NPR and available  $C_m$ .

## 5. Thrust vectoring of manipulated jet

It is of interest to examine thrust vectoring, which can improve aircraft manoeuvrability (Zigunov *et al.* 2022). As discussed in § 4.1, minijet injection may display a thrust vectoring phenomenon, where the main jet deflects away from the jet centreline. This phenomenon can be quantified in terms of thrust vector angle  $\delta$  based on the deviation of the maximum Pitot pressure from the centreline for  $3 \leq x^* \leq 15$  (Zigunov *et al.* 2022). The uncertainty in  $\delta$ , estimated using the propagation of errors (Moffat 1985), is within  $\pm 0.1^\circ$ . Alternatively, we may identify a series of shock crossover locations, as illustrated in figure 16(d), in the schlieren images based on the pixel level and then estimate  $\delta$  using a linear fit to these crossover locations. Following Athira *et al.* (2020), the images were calibrated to  $0.11 \text{ mm pixel}^{-1}$  so that the maximum spatial uncertainty in determining these crossover locations is  $0.5 \text{ mm}$ , producing an uncertainty in  $\delta$  within  $\pm 0.2^\circ$ . The two estimates in  $\delta$  agree reasonably well with each other (figure 15). Hereinafter, we present  $\delta$  estimated from schlieren images.

The dependence of  $\delta$  on  $C_m$  is presented in figure 15. In general,  $\delta$  increases almost linearly with increasing  $C_m$ . For  $d/D = 1/20$ ,  $\delta$  is negligibly small probably because of small  $C_m$  ( $< 1\%$ ). Recall our observation in figure 8 that jet mixing is enhanced little at  $d/D = 1/20$ . It may be inferred that the jet perturbation is insignificant if  $d/D$  is very small, i.e.  $d/D \leq 1/20$ . On the other hand,  $\delta$  can be markedly larger for  $d/D = 1/5.3$  than for other  $d/D$  as  $C_m$  is quite large.

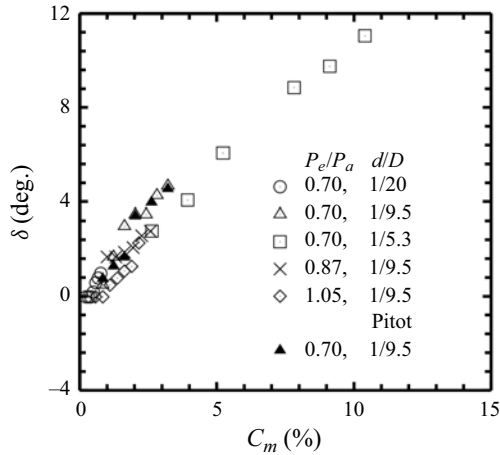


Figure 15. Dependence on mass flow rate ratio  $C_m$  of thrust vector angle  $\delta$  estimated from schlieren images and Pitot pressure ratio data for various  $P_e/P_a$  and  $d/D$ .

One interesting observation is that, given  $d/D$  and  $C_m$ ,  $\delta$  is smaller at  $P_e/P_a = 1.05$  than at  $P_e/P_a = 0.70$  or  $0.87$ . For example,  $\delta$  is  $3.5^\circ$  at  $P_e/P_a = 0.70$  but only  $1.8^\circ$  at  $P_e/P_a = 1.05$  despite the same  $d/D$  ( $= 1/9.5$ ) and  $C_m$  ( $= 1.98\%$ ). This suggests jet vectoring is more appreciable under the off-design condition than under the design condition, in distinct contrast to jet mixing that is more readily enhanced under the design condition than under the off-design condition (figure 8). We present in figure 16 the time-averaged schlieren images of the manipulated jet at  $P_e/P_a = 0.70$  and  $1.05$  ( $d/D = 1/9.5$ ) along the  $xz$  and  $xy$  planes for  $C_m = 0.79\%$ – $1.98\%$ . Several observations can be made. Firstly, the minijet injection along the  $z$  direction makes the jet deflect towards the negative  $z$  direction (figure 16*b,d,f*), producing thrust vectoring in addition to enhancing jet mixing. As one may expect, there is no appreciable jet deflection in the  $xy$  plane (figure 16*c,e,g*). Secondly, as the *IPR* exceeds 2 (table 2), the minijet is supersonic and choked (Perumal & Zhou 2018). This minijet penetrates into the main jet and modifies the shock structure near the nozzle exit, as indicated by the induced oblique shock (figure 16*h*) towards the negative  $z^*$  direction (figure 16*b,d,f,h*). However, the oblique shock wave from the other side of the nozzle lip (figure 16*b*) remains similar to that of the natural jet, suggesting that the minijet fails to penetrate through the main jet. Thirdly, a close-up examination of the first shock cell reveals a potential source for jet deflection, i.e. the oblique shock wave, which is then reflected as expansion fans from the jet shear layer (Perumal & Rathakrishnan 2013). It is well known that a supersonic flow may be turned away from the centreline due to the presence of expansion fans, resulting in jet vectoring (Anderson 1982). This implies a correlation between  $\delta$  and expansion fans, which depends on  $\beta$ . As noted from figure 11,  $\beta$  is enlarged with increasing  $C_m$ ; so is  $\delta$ . Finally,  $\beta$  decreases from  $P_e/P_a = 0.70$  to  $1.05$  given  $C_m = 1.98\%$  (figure 16*f,h*). The smaller  $\beta$  at  $P_e/P_a = 1.05$  leads to a small deflection angle or  $\delta$  from the expansion fans (figure 16*a*). As a result, the main jet is forced to swing towards the centreline, thus reducing  $\delta$  at  $P_e/P_a = 1.05$  (figure 16*a*). A similar observation on jet turning towards its axis was also reported by Neely, Gesto & Young (2007).

It is of interest to compare how  $\beta$  and  $L_c^*$  vary with  $\delta$ . As shown in figure 17(*a*),  $\beta$  is in general positively correlated to  $\delta$  since  $\beta$  is primarily responsible for jet deflection. The dependence of  $\beta$  on  $\delta$  displays two branches. The value of  $\beta$  increases gradually with  $\delta$  at  $P_e/P_a = 0.70$  but rather rapidly for  $P_e/P_a = 0.87$ – $1.05$ . Further,  $L_c^*$  decreases with an increase in  $\delta$  and again shows two branches, slowly decreasing at  $P_e/P_a = 0.70$  but

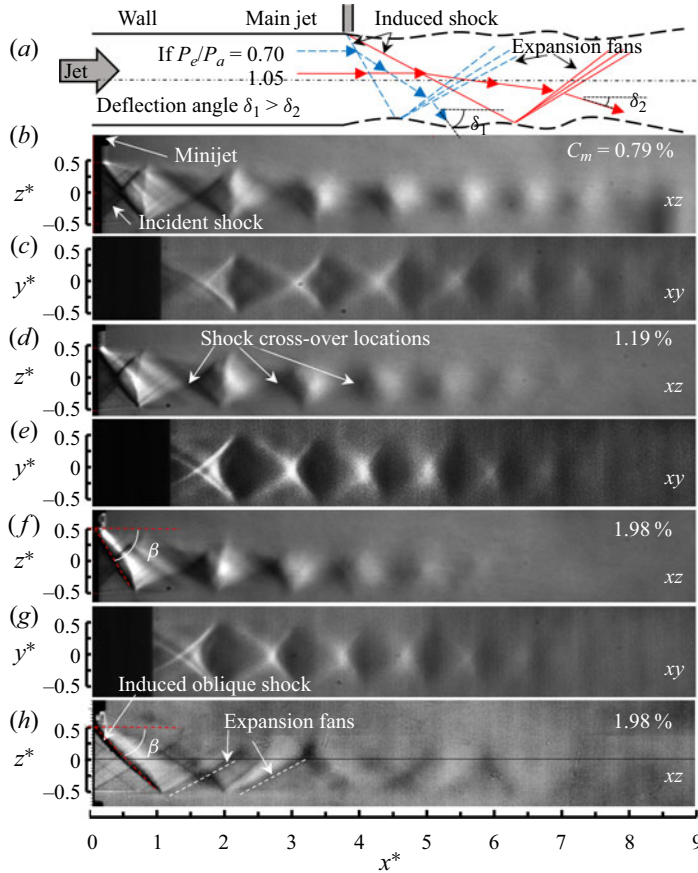


Figure 16. (a) Sketch of induced shocks and expansion fans; blue and red correspond to  $P_e/P_a = 0.70$  and 1.05, respectively. (b–g) Time-averaged schlieren images of the manipulated jet ( $d/D = 1/9.5$ ) captured in two orthogonal planes at  $P_e/P_a = 0.70$  and (h) at  $P_e/P_a = 1.05$ .

more rapidly for  $P_e/P_a = 0.87$ –1.05 in figure 17(b). Evidently, while enhancing jet mixing, the minijet injection may also induce jet vectoring, which may be undesirable for some applications, e.g. during a certain phase of flight.

It has been well established that the penetration depth of the minijet into the main jet dictates the vectoring angle (Neely et al. 2007; Warsop & Crowther 2018; Wu, Kim & Kim 2020). Chandra Sekar et al. (2021) investigated jet thrust vectoring via secondary fluidic injection and proposed that  $\delta$  may scale with  $\rho_i U_i^2 / (\rho_j U_j^2)$ . Their investigation did not consider the possible effects of  $P_e/P_a$  and  $d/D$ . In view of  $L_c^* = f_6(\xi)$  and also the correlation between  $L_c^*$  and  $\delta$  (figure 17b), one may wonder whether  $\delta$  is also correlated with  $\xi$  ( $= (Jd_i/D_j) / (\gamma M_j^2 P_e/P_a)$ ). To our surprise, the  $\delta$  data in figure 15 fall about one curve once  $\xi$  is used as abscissa, as shown in figure 18(a), irrespective of  $P_e/P_a$ ,  $d/D$  and  $C_m$ . The curve may be divided into two zones, namely the dead and linear zones, corresponding to  $\xi \leq 0.02$  and  $\xi > 0.02$ , respectively. In the dead zone,  $\delta \approx 0$  and the jet is not deflected, as illustrated in figure 18(b). On the other hand, the data may be fitted in the linear zone to

$$\delta = 88\xi - 1.76, \quad (5.1)$$

and the jet is deflected, as shown in figure 18(c). Evidently,  $\delta$  is linearly correlated to  $\xi$ .

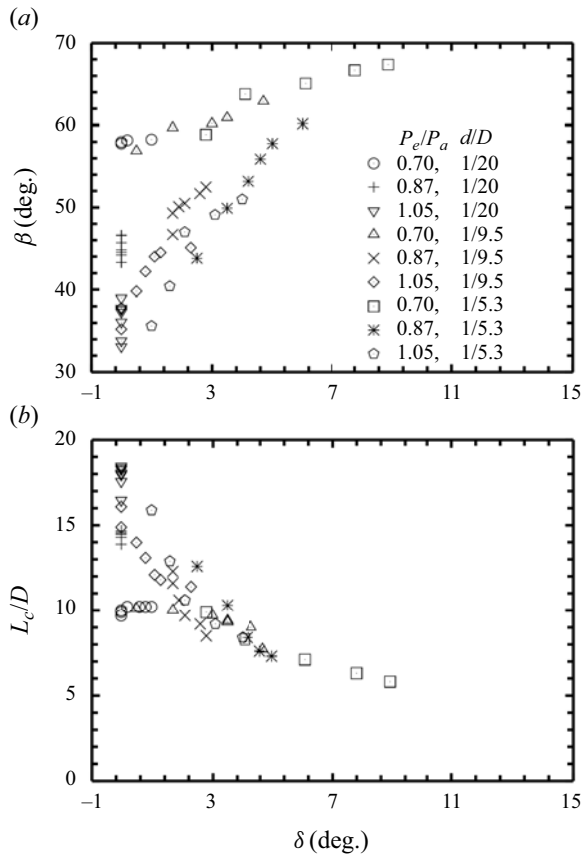


Figure 17. Dependence on thrust vector angle  $\delta$  of (a) shock wave angle  $\beta$  and (b) supersonic core length  $L_c/D$  for  $P_e/P_a = 0.70$ – $1.05$  and  $d/D = 1/20$ – $1/5.3$ .

## 6. Flow structure of manipulated jet

To understand the minijet-generated flow structure, we present instantaneous schlieren images of the manipulated jet for  $NPR = 1.9$ – $4.0$  given  $IPR = 7.0$  and  $d/D = 1/6.5$ , corresponding to  $C_m = 12.73\%$ – $6.04\%$ , in figure 19(a–e). Note that  $NPR$  is the only parameter that changes, which causes  $C_m$  ( $\sim (IPR/NPR)(d/D)^2$ ) to vary as given in (2.5)–(2.6). Interestingly, the images show unequivocally the occurrence of a quasi-periodical vortex street. The vortices, as indicated by the shadows, grow in size and their trajectory may cross over the centreline further downstream. Furthermore, the minijet penetration depth, as indicated by the trajectory of the vortices, retreats with decreasing  $C_m$ . However, the vortex street disappears once  $C_m = 0$ . Figure 19(f) shows the schlieren image from the jet ( $P_e/P_a = 0.70$ ,  $d/D = 1/6.5$ ) manipulated by a dummy minijet, that is, a minijet nozzle with an outer diameter  $d_{out}/D = 1/4.8$  is placed in the jet, whose lower end is at  $x^* = 0.2$  and  $z^* = 0.3$ , the same as in figure 19(a–e), though without injecting any fluid ( $C_m = 0$ ). The  $NPR$  is the same as in figure 19(e). The dummy minijet produces similar shock-cell structures in the near field to those in figure 19(e). However, the vortex street is absent in figure 19(f). Apparently, the minijet injection is essential for the street to take place.

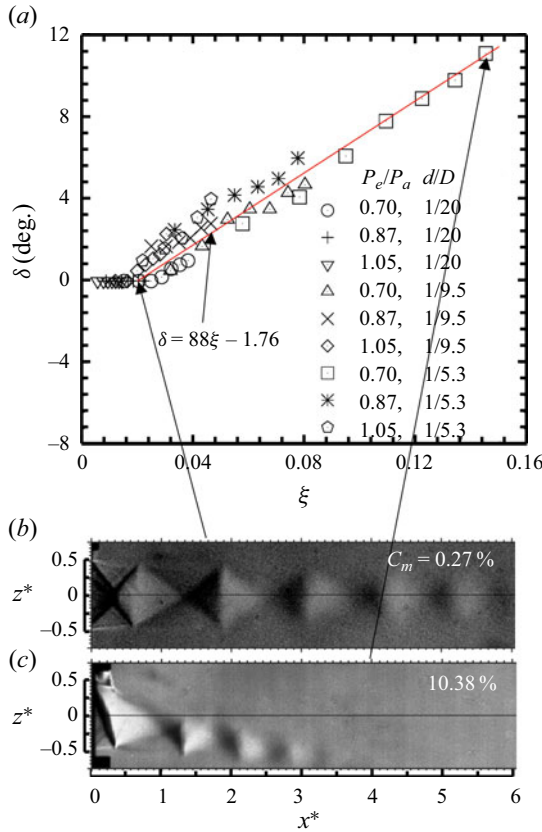


Figure 18. (a) Dependence of  $\delta$  on  $\xi$  ( $C_m = 0.18\text{--}10.38\%$ ). (b,c) Schlieren images for  $\xi = 0.021$  in the dead zone ( $P_e/P_a = 0.70$ ,  $d/D = 1/9.5$ ,  $C_m = 0.27\%$ ) and 0.15 in the linear region (0.70, 1/5.3, 10.38%).

To understand the flow structure captured in the time-resolved schlieren images, we employ the proper orthogonal decomposition (POD) technique to analyse the organized and energetic structures. The snapshot POD method proposed by Sirovich (1987) is used to obtain the POD modes. Briefly, given  $r$  snapshots of the flow field with an equal time interval  $\Delta t$ , the spatiotemporal field may be divided into time-dependent coefficients and the optimal basis functions. Snapshot POD satisfies the following condition:

$$X = [\mathbf{x}_1 \mathbf{x}_2 \dots \mathbf{x}_r] \in \mathbb{R}^{n \times r}, \quad n \gg r. \quad (6.1)$$

The data of  $r$  ( $= 500$ ) snapshots are stacked into a matrix  $X$ , and  $\mathbf{x}_k$  ( $k = 1, 2, \dots, r$ ) in the vector space  $\mathbb{R}^n$  corresponds to the grey value of all pixels in one schlieren image (Taira *et al.* 2017). There are presently  $512 \times 128$  pixels, i.e.  $n = 65\,536$  grey values per image. The autocovariance matrix is then created as  $X^T X \in \mathbb{R}^{r \times r}$ , and the corresponding eigenvalue problem  $X^T X \boldsymbol{\psi}_j = \lambda_j \boldsymbol{\psi}_j$  yields the eigenvalues  $\lambda_j$  ( $\lambda_1 > \lambda_2 > \dots > \lambda_r$ , for  $j = 1, 2, \dots, r$ ) and eigenvectors  $\boldsymbol{\psi}_j \in \mathbb{R}^r$  from which the spatial POD modes are constructed as

$$\boldsymbol{\phi}_j = X \boldsymbol{\psi}_j \frac{1}{\sqrt{\lambda_j}} \in \mathbb{R}^n, \quad j = 1, 2, \dots, r. \quad (6.2)$$



## A minijet-manipulated supersonic jet

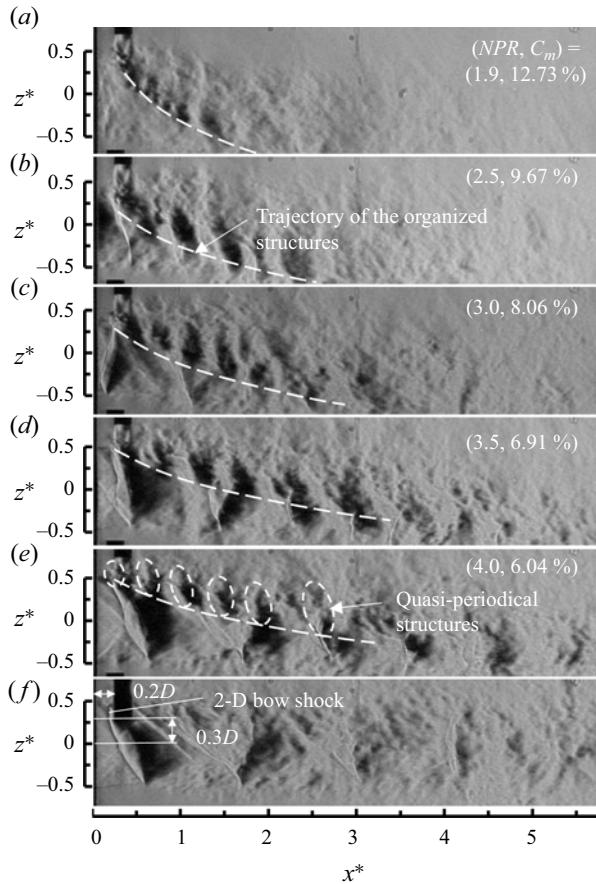


Figure 19. Instantaneous schlieren images captured at 43 kHz: (a–e) manipulated jet at  $d/D = 1/6.5$  and  $IPR = 7.0$ ; (f)  $C_m = 0$  with the minijet nozzle protruding into the jet ( $x^* = 0.2$ ,  $z^* = 0.3$ ). The broken curve indicates the trajectory of the organized structures.

The temporal coefficient  $a$  is determined by projecting  $X$  onto the spatial POD modes  $\phi_j$  and can be expressed at time  $k$  for each mode  $j$  as

$$a_j(k) = \phi_j x_k. \quad (6.3)$$

The eigenvalues  $\lambda_j$  of the POD modes are arranged in the order of importance in terms of the fluctuating energy of the flow field, and can be calculated as

$$\frac{\lambda_j}{\sum_1^r \lambda_j}. \quad (6.4)$$

Finally, to describe the coherent structures more accurately, the snapshots are de-averaged before being assembled into matrix  $X$ . Then the POD method is applied to analyse the remaining data (Rao, Kushari & Mandal 2020). Note that the input matrix  $X$  is composed of the grey values of the entire ensemble of instantaneous schlieren images.

Figure 20 shows typical instantaneous and time-averaged schlieren images along with the reconstructed images of the first eight POD modes ( $P_e/P_a = 0.87$ ,  $d/D = 1/5.3$ ,  $C_m = 5.19\%$ ) calculated from 300 schlieren images captured at a sampling rate of 43 kHz. The white- and black-coloured regions result from a variation in the density of flow.

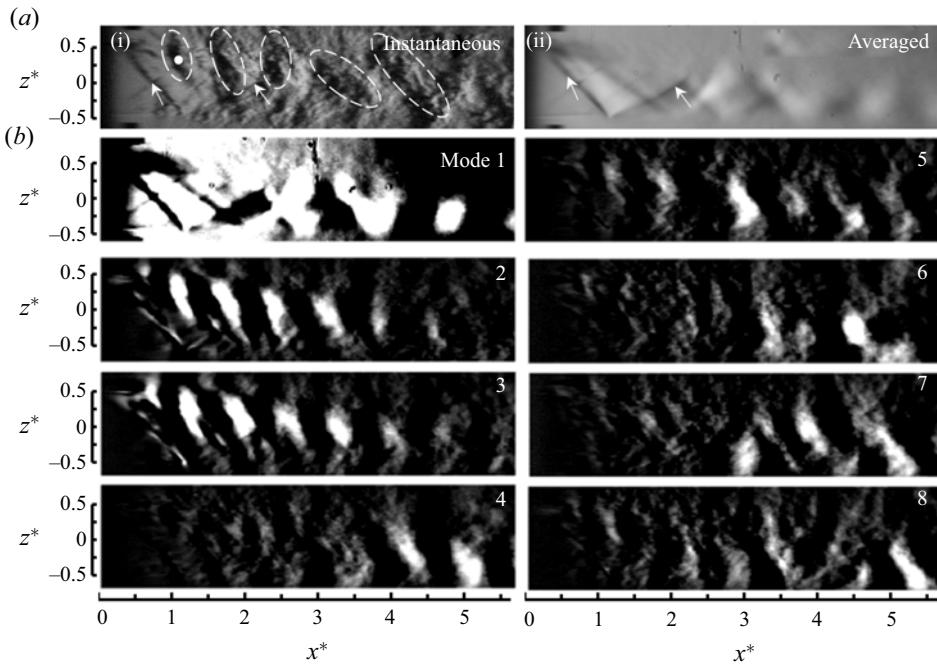


Figure 20. (a) (i) Instantaneous and (ii) averaged schlieren images of the manipulated jet for  $P_e/P_a = 0.87$ ,  $d/D = 1/5.3$  and  $C_m = 5.19\%$  when the minijet is placed at  $x/D = 0.2$ . (b) Reconstructed images of the first eight POD modes calculated from 300 schlieren images captured at a sampling rate of 43 kHz. Arrows in (ai,aii) point to the induced shocks or expansion fans, and the ellipses in (ai) highlight the flow structures that occur downstream of the minijet.

The low-density regions correspond to high grey values and hence white colour, while the high-density regions result in a grey value of near zero and hence black colour. The minijet-induced oblique shock and its reflections are evident, as indicated by the arrows in figure 20(ai,aii). A series of quasi-periodical structures are visible downstream of the minijet in the instantaneous image, as highlighted by ellipses in figure 20(ai). Mode 1 displays apparently the distorted shock cells, which is evident in both instantaneous and time-averaged schlieren images (figure 20ai,aii). The structures shown in modes 2–3 appear to be quasi-periodical and do not change significantly in topology, which is different from those in modes 1 and 4–8. These quasi-periodical structures obviously correspond to those noted in the instantaneous schlieren image. Modes 4–8 are distinct from modes 2–3 and do not correspond to quasi-periodical structures. The cumulative energies of modes 1–3 and 2–3 account for more than 40% and 6%, respectively, of the total energy (not shown). When advected downstream, these quasi-periodical structures grow gradually in size and interact with the shock waves, distorting the shock cells and contributing to rapid jet mixing. The observations are confirmed by the power spectral density (PSD) functions of the POD coefficients; a pronounced peak is evident at  $St_e = f_e D_j / U_j = 0.12$  for modes 2–3 but absent for modes 4–8 (figure 21a), where  $f_e$  is the frequency of quasi-periodical structures. Note that this peak is also observed in the PSD function of the grey values taken at  $((x^*, z^*) = (1, \frac{1}{4}))$  (figure 20ai), pointing to the correspondence between this peak and the quasi-periodical structures. The phase plot of the POD coefficients  $a_2$  and  $a_3$  of modes 2 and 3 may provide us with the information on the temporal correlation between the two modes, where the data points fall approximately within a circle (figure 21b).

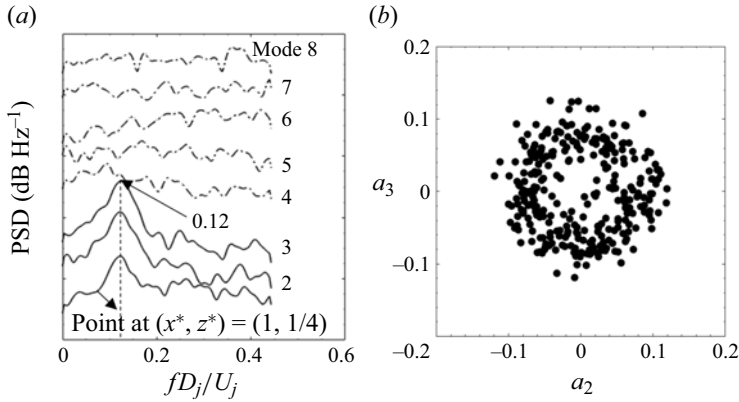


Figure 21. (a) The PSD function of POD coefficients for modes 2–8 and PSD function of grey values for location  $(x^*, z^*) = (1, \frac{1}{4})$ , as shown in figure 20(ai). (b) Phase plot of the POD coefficients of modes 2–3.

Along with their similar topology as shown in figure 20(b), the result indicates their collective representation of an oscillatory process for the quasi-periodical structures. As such, we present the data of only mode 2 for further discussion.

The predominant frequency  $St_e$  exhibits a significant dependence on  $C_m$ ,  $d/D$  and  $P_e/P_a$ . As illustrated in figure 22,  $St_e$  decreases with increasing  $C_m$ , regardless of  $P_e/P_a$  and  $d/D$ . For a given  $U_i/U_j$ , an increase in  $d/D$  leads to a significant decrease in  $St_e$ . For example, at  $P_e/P_a = 0.70$  and  $U_i/U_j = 1.1$ ,  $St_e$  is 0.2 for  $d/D = 1/6.5$  but 0.1 for  $d/D = 1/5.3$ . On the other hand, given  $d/D$  and  $C_m$ ,  $St_e$  declines from  $P_e/P_a = 0.87$  to 0.70. One important question arises. Can we find a dimensionless parameter with which  $St_e$  scales? Note that both  $L_c^*$  and  $\delta$  scale with  $(Jd_i/D_j)/(\gamma M_j^2 P_e/P_a)$ . After careful analysis of the experimental data in figure 22 along with numerous trial-and-error attempts, we find that, once the abscissa in figure 22 is replaced by  $\zeta = J(d_i/D_j) \sqrt{\gamma M_j^2 P_e/P_a}$ , the  $St_e$  data collapse reasonably well about one curve, as shown in figure 23:

$$St_e = 3.60e^{-8\zeta} + 0.02. \quad (6.5)$$

As noted earlier,  $(J(d_i/D_j))^2 = C_m U_i/U_j$  is the momentum ratio of the minijet to the main jet. On the other hand,  $P_e/P_a$  (see (2.2)) provides a measure for the degree of departure from the design condition. Apparently,  $P_e/P_a \rightarrow 0$  implies  $\zeta \rightarrow 0$  for given  $J(d_i/D_j)$ . Recall the inference in §4.1 that the manipulated jet at  $P_e/P_a \approx 1$  experiences a more pronounced reduction in  $L_c^*$  than at smaller  $P_e/P_a$ , which suggests a less effective manipulation under off-design conditions ( $P_e/P_a \rightarrow 0$ ) than under the design condition ( $P_e/P_a \rightarrow 1$ ) for given  $C_m$  or  $J(d_i/D_j)$ . Noting  $J(d_i/D_j) = \sqrt{MR_N}$ ,  $\zeta = \sqrt{MR_N} \sqrt{\gamma M_j^2 P_e/P_a} = \sqrt{\rho_i U_i^2 / \rho_j U_j^2 (d_i/D_j)} \sqrt{\rho_j U_j^2 / P_a} = \sqrt{\rho_i U_i^2 / P_a (d_i/D_j)} = \sqrt{\rho_i U_i^2 (\pi d_i^2 / 4)} / \sqrt{P_a (\pi D_j^2 / 4)}$ . Applying the jet thrust equation, derived from the momentum equation by Anderson (1982), to the present main jet yields  $\rho_j U_j^2 (\pi D_j^2 / 4) + (\pi D_j^2 / 4) (P_e - P_a)$ , where  $\rho_j U_j^2 (\pi D_j^2 / 4)$  is the momentum thrust and  $(\pi D_j^2 / 4) (P_e - P_a)$  is the pressure thrust due to a difference between the jet pressure and ambient pressure. Apparently,  $\sqrt{\rho_i U_i^2 (\pi d_i^2 / 4)}$  is the momentum thrust of the minijet and  $\sqrt{P_a (\pi D_j^2 / 4)}$  is the

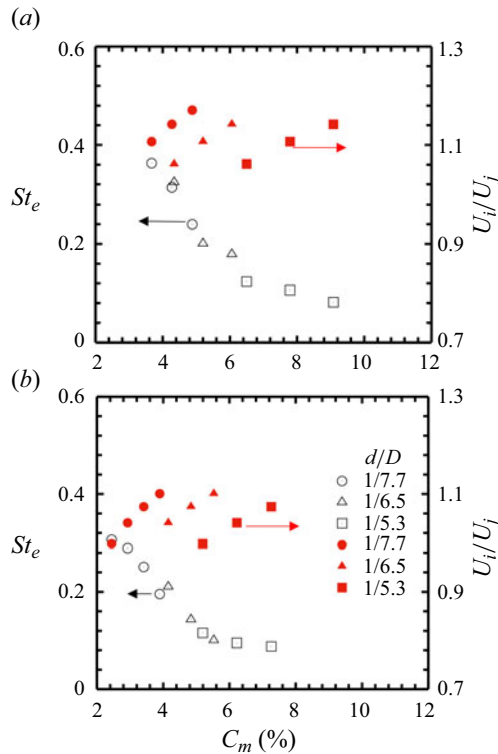


Figure 22. Dependence on  $C_m$  of the predominant frequency  $St_e = f_e D_j / U_j$  of the observed vortex street and correlation between  $U_i/U_j$  and  $C_m$ : (a)  $P_e/P_a = 0.70$ , (b) 0.87.

thrust produced by ambient pressure or a reference thrust. Then,  $\zeta$  may be interpreted as the ratio of the minijet momentum thrust to the ambient pressure thrust.

Figure 24 compares instantaneous schlieren images at various  $C_m$  for  $d/D = 1/9.5$  and  $1/7.7$  ( $P_e/P_a = 1.05$ ,  $M_j = 1.83$ ) along with the corresponding PSD functions of the POD coefficients for mode 2. In the absence of control ( $C_m = 0$ ), one prominent peak occurs at  $St_0 \approx 0.21$  in the PSD function (figure 24ai), suggesting a natural instability. The schlieren image of the natural jet displays staggered structures (figure 24ai), as highlighted by the white dashed ellipses, which are also captured in the POD mode 2 of schlieren images (not shown). Such structures were observed in screeching jets by Powell (1953) and Panda (1998), as shown in their figures 7 and 3, respectively. Furthermore,  $St_0$  may be reasonably well predicted by Tam, Seiner & Yu's (1986) semi-theoretical formula for screeching jets ( $St_0 = 0.22$  for  $M_j = 1.83$ ). The evidence points to the occurrence of the screeching mode in the natural jet at  $M_j = 1.83$ . However, this peak disappears under control given  $d/D = 1/9.5$  and  $C_m \leq 2.11\%$  (figure 24b) and remains so for a further increase in  $C_m$ . Once  $d/D$  increases to  $1/7.7$  and  $C_m \geq 2.02\%$ , one prominent peak appears again at  $St_e \approx 0.18$  at  $C_m = 3.24\%$ . The prominent peak cannot be detected until  $C_m$  exceeds a threshold, which is  $2.02\%$ ,  $4.03\%$  and  $4.33\%$  for  $d/D = 1/7.7$ ,  $1/6.5$  and  $1/5.3$ , respectively, but not observed for  $d/D = 1/9.5$ . A similar observation is made for other  $P_e/P_a$ ; the threshold of  $C_m$  for the occurrence of this peak is about  $3.04\%$ ,  $2.43\%$  and  $2.02\%$  for  $P_e/P_a = 0.70$ ,  $0.87$  and  $1.05$  (for  $d/D \geq 1/7.7$ ), respectively.

One may wonder as to the physical mechanism behind the generation of the quasi-periodical structures with  $St_e$ . Do they originate from the main jet or from

### A minijet-manipulated supersonic jet

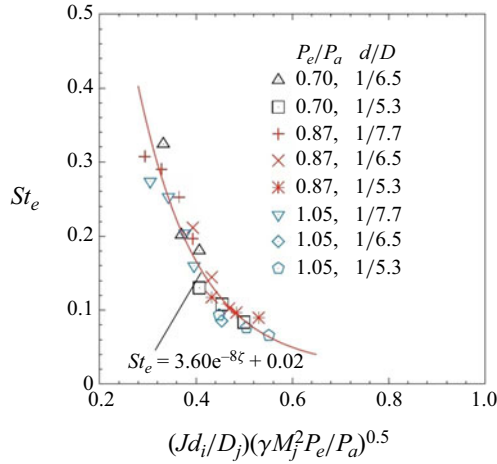


Figure 23. Dependence of  $St_e$  on the scaling factor  $\zeta = J(d_i/D_j) \sqrt{\gamma M_j^2 P_e/P_a}$ . The solid curve is the least-squares fitting to experimental data.

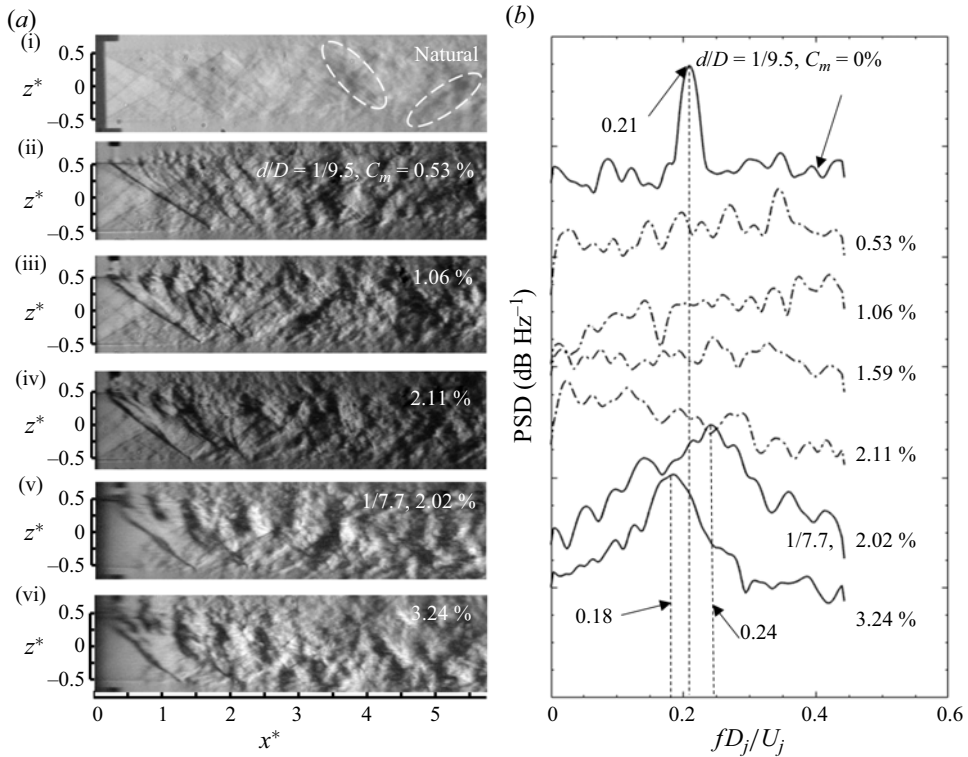


Figure 24. (a) Instantaneous schlieren images ( $P_e/P_a = 1.05, M_j = 1.83$ ): (i) natural jet; manipulated jet for (ii–iv)  $d/D = 1/9.5$  and (v,vi)  $1/7.7$ . (b) Corresponding PSD functions of POD coefficients for mode 2.

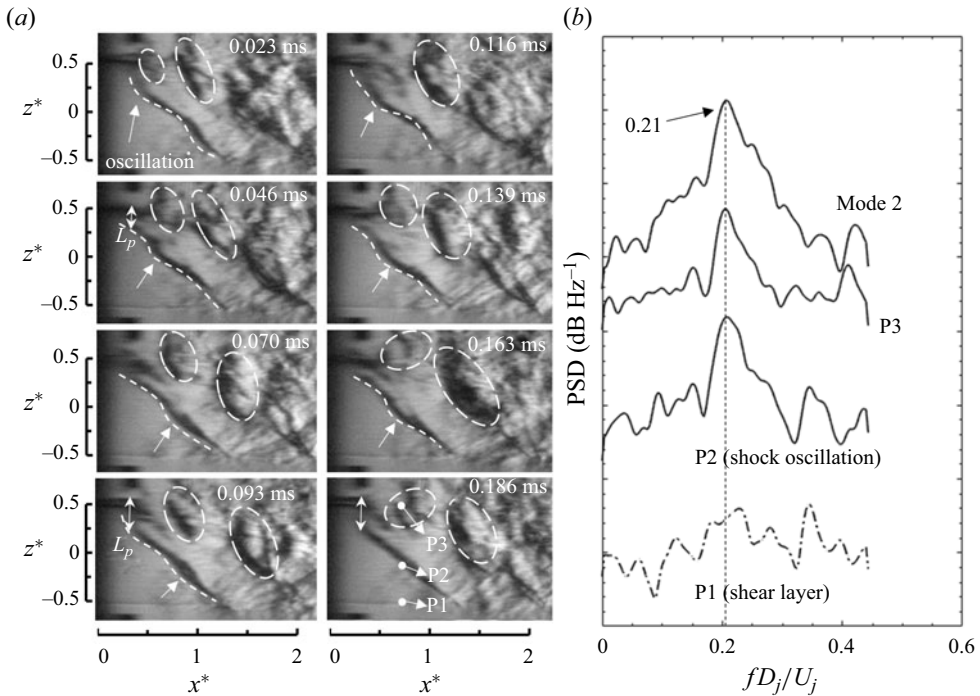


Figure 25. (a) Sequential schlieren images of the manipulated jet ( $P_e/P_a = 1.05$ ,  $d/D = 1/7.7$ ,  $C_m = 2.83\%$ ). (b) The PSD functions of POD coefficients of mode 2, calculated from the entire flow field and the grey values from three representative points P1, P2 and P3, as indicated in (a). The elliptic contours highlight the occurrence of the quasi-periodical vortices.

the minijet? The scaling law (figure 23) is related to the parameters  $D_j$ ,  $U_j$  and  $M_j$  of main jet along with  $d_i$  and  $C_m$  of the minijet, suggesting a link to both minijet and main jet. We present eight sequential schlieren images of the manipulated jet in figure 25(a), along with the PSD functions of the POD coefficients for mode 2 from the flow field shown in the bottom-right panel of figure 25(a) and the grey values from three points P1, P2 and P3 in the shear layer, at the edge of the bow shock and inside the vortex street, respectively (figure 25b). The quasi-periodical vortices are highlighted by elliptic contours and correspondingly one prominent peak occurs at  $St_e \approx 0.21$  in the PSD function (the upper curve of figure 25b). A careful examination of the images reveals that the bow shock oscillates, as indicated by the arrows. The spectra obtained at P2 and P3 display a pronounced peak at  $St_e \approx 0.21$  but not at P3 (figure 25b), that is, the predominant frequency of the quasi-periodical structures is the same as the oscillating frequency of the bow shock, but this frequency could not be detected in the shear layer. Furthermore, both instantaneous  $L_p$  and  $\beta$  change, the latter being not marked in figure 25(a). For example,  $L_p$  contracts at 0.046 (ms) and is prolonged at 0.093 (ms). As discussed previously,  $L_p$  and  $\beta$  are linked to the minijet penetration depth.

Based on the above observations, one scenario is proposed for the physical mechanism behind the occurrence of the quasi-periodical vortex street. The jet is associated with a natural instability characterized by  $f_0$  or  $St_0$ . Under control, the minijet injection interacts with the oscillating bow shock. This instability can be suppressed when  $C_m$  is small but excited and amplified once  $C_m$  exceeds a threshold, which leads to the occurrence of the

quasi-periodical vortex street and meanwhile  $St_0$  changes to  $St_e$ , which scales with the momentum ratio  $\zeta$  (figure 23).

## 7. Conclusions

Experimental investigation has been conducted to study the jet mixing enhancement of a supersonic axisymmetric jet with a design Mach number  $M_d = 1.8$ . The jet is manipulated using a single steady radial minijet at the design and off-design conditions, corresponding to  $P_e/P_a = 1$  and  $P_e/P_a \neq 1$ , respectively. Two important minijet parameters are investigated, namely the mass flow rate ratio  $C_m$  or velocity ratio  $U_i/U_j$  and diameter ratio  $d/D$  of the minijet to the main jet. Detailed pressure and flow visualization measurements are carried out using a Pitot tube and schlieren technique, respectively. The following conclusions can be drawn out of this work.

- (i) Jet mixing, quantified via the core length  $L_c^*$ , of the manipulated supersonic jet exhibits a strong dependence on  $C_m$  (or  $U_i/U_j$ ),  $d/D$ ,  $P_e/P_a$  and  $M_j$ . Length  $L_c^*$  retreats with increasing  $C_m$  for all  $P_e/P_a$ , suggesting an increased jet mixing rate with increased minijet penetration depth into the main jet. So does  $L_c^*$  with decreasing  $d/D$  for a given  $C_m$ , which also acts to increase the minijet penetration depth. With an increase in  $P_e/P_a$ ,  $L_c^*$  retreats markedly with respect to a natural jet and the maximum reduction in  $L_c^*$  occurs at  $P_e/P_a = 1$  for given  $C_m$  and  $d/D$ . This retreat is ascribed to a larger penetration depth due to the weak shock cell strength formed under the design condition ( $P_e/P_a \approx 1$ ), as compared to the strong shock cell strength under the off-design condition ( $P_e/P_a \neq 1$ ).
- (ii) Empirical scaling analysis performed on experimental data along with the fully expanded jet Mach number  $M_j$  reveals that  $L_c^* = f_1(C_m, d/D, P_e/P_a, M_j)$  may be reduced to  $L_c^* = f_2(\xi)$ . The scaling factor  $\xi = J(d_i/D_j)/(\gamma M_j^2 P_e/P_a)$  is physically the penetration depth of the minijet into the main jet, where  $J(d_i/D_j) = \sqrt{C_m U_i/U_j} = \sqrt{\rho_i U_i^2 / (\rho_j U_j^2)} (d_i/D_j)$  ( $C_m U_i/U_j$  is the momentum ratio of minijet to main jet or penetration depth) and  $\gamma M_j^2 P_e/P_a$  is the non-dimensional exit pressure ratio that characterizes a natural jet (e.g. Driftmyer 1972). This scaling law is more general than  $L_c^* = f(\sqrt{MR_N}/(\gamma M_j^2 P_e/P_a))$  developed by Perumal & Rathakrishnan (2022) and Khan *et al.* (2022) who used 2 and 2–6 minijets, respectively. Their scaling law is valid only for a fixed  $d/D$ , whilst the present scaling law is valid not only for different  $M_d$  but also for varying  $d/D$ . The optimal  $d/D$  and required  $C_m$  may be estimated from the scaling law, given a predefined  $L_c^*$ ,  $\gamma$  and  $M_j$ , in the case of  $IPR = NPR$  ( $NPR$  and  $IPR$  are related to  $U_j$  and  $U_i$ , respectively). Further, the scaling law highlights that the choice of the optimal  $d/D$  is a trade-off among the minimum operating  $M_j$ , required jet mixing and available  $C_m$ . This is in distinct contrast to a subsonic jet where the optimal  $d/D$  is a trade-off between required jet mixing and available  $C_m$  (Perumal & Zhou 2021).
- (iii) It has been found that, once  $d/D \geq 1/7.7$  and  $C_m$  exceeds a certain level for a given exit pressure ratio (e.g.  $C_m \geq 3.04\%$ ,  $2.43\%$  and  $2.02\%$  for  $P_e/P_a = 0.70$ ,  $0.87$  and  $1.05$ , respectively), the minijet may generate a street of quasi-periodic large-scale structures downstream. This street exhibits a strong dependence on  $C_m$  or  $U_i/U_j$ ,  $d/D$  and  $P_e/P_a$  (figure 22) and the dimensionless frequency  $St_e$  ( $\equiv f_e D_j/U_j$ ) of the structures scales with a factor  $\zeta = J(d_i/D_j) \sqrt{\gamma M_j^2 P_e/P_a}$  (figure 23), where  $\zeta$  is physically the ratio of the minijet momentum thrust to the ambient pressure thrust.

The formation mechanism of the large-scale structure street is different from that of the Kármán vortex street generated behind a cylinder in cross-flow.

- (iv) The thrust vectoring angle  $\delta$  that takes place under the minijet manipulation depends strongly on  $C_m$ ,  $d/D$  and  $P_e/P_a$  and also scales with  $\xi$ , that is,  $\delta = f_3(C_m, d/D, P_e/P_a)$  may be reduced to  $\delta = f_4(\xi)$ . Naturally,  $\delta$  is also correlated with  $L_c^*$  (figure 17b), implying that jet mixing grows with increasing jet deflection.

## Nomenclature

$P_{0s}$	stagnation pressure in the settling chamber (bar)
$P_{0t}$	total pressure measured by the Pitot tube (bar)
$P_a$	atmospheric pressure (bar)
$P_e$	static pressure at the nozzle exit of the main jet (bar)
$NPR$	nozzle pressure ratio of the main jet, $P_{0s}/P_a$
$IPR$	injection pressure ratio of the minijet, $P_{0s,i}/P_a$
$M_d$	design Mach number of the main jet
$M_j$	fully expanded jet Mach number of the main jet
$d$	nozzle exit diameter of minijet (mm)
$d_i$	fully expanded diameter of minijet (mm)
$D$	nozzle exit diameter of main jet (mm)
$D_{th}$	nozzle throat diameter of main jet (mm)
$D_j$	fully expanded diameter of main jet (mm)
$\dot{m}_i$	mass flow rate of minijet ( $\text{kg s}^{-1}$ )
$\dot{m}_j$	mass flow rate of main jet ( $\text{kg s}^{-1}$ )
$U_i$	exit velocity of minijet ( $\text{m s}^{-1}$ )
$U_j$	exit velocity of main jet ( $\text{m s}^{-1}$ )
$C_m$	mass flow rate ratio of minijet to main jet, $\dot{m}_i/\dot{m}_j$
$J$	momentum flux ratio or effective velocity ratio of minijet to main jet, $\sqrt{\rho_i U_i^2 / (\rho_j U_j^2)}$
$MR$	total momentum ratio of minijet to main jet, $C_m U_i / U_j$
$\delta$	thrust vector angle or deflection angle (deg.)
$L_c^*$	supersonic core length, normalized by $D$
$L_p^*$	penetration depth, normalized by $D$
$St_0$	normalized frequency of large-scale structures in natural jet, $f_0 D_j / U_j$
$St_e$	normalized frequency of large-scale structures in manipulated jet, $f_e D_j / U_j$

**Funding.** Y.Z. wishes to acknowledge support from China Guangdong Nuclear Power Corporation through grant CGN-HIT202221 and from the Research Grants Council of the Shenzhen Government through grant JCYJ20210324132816040.

**Declaration of interests.** The authors report no conflict of interest.

### Author ORCIDs.

-  Changhao Tan <https://orcid.org/0009-0005-2612-169X>;  
 Arun Kumar Perumal <https://orcid.org/0000-0002-0547-5609>.

## REFERENCES

- AKRAM, S., PERUMAL, A.K. & RATHAKRISHNAN, E. 2021 Effect of tab parameters on the near-field mixing characteristics of a Mach 1.5 elliptic jet. *Phys. Fluids* **33** (3), 03611.



## *A minijet-manipulated supersonic jet*

- ANDERSON, D.A., TANNEHILL, J.C. & PLETCHER, R.H. 1984 *Computational Fluid Mechanics and Heat Transfer*. Hemisphere Publishing.
- ANDERSON, J.D. 1982 *Modern Compressible Flow with Historical Perspective*. McGraw Hill Book Company.
- ANDRÉ, B., CASTELAIN, T. & BAILLY, C. 2013 Experimental exploration of under-expanded supersonic jets. *Shock Waves* **24**, 21–32.
- ATHIRA, C.M., RAJESH, G., MOHANAN, S. & PARTHASARATHY, A. 2020 Flow interactions on supersonic projectiles in transitional ballistic regimes. *J. Fluid Mech.* **894**, A27.
- CALLENDER, B., GUTMARK, E. & MARTENS, S. 2007 A comprehensive study of fluidic injection technology for jet noise reduction. In *13th AIAA/CEAS Aeroacoustics Conference (28th AIAA Aeroacoustics Conference)*. AIAA.
- CATTAFESTA, L.N. & SHEPLAK, M. 2011 Actuators for active flow control. *Annu. Rev. Fluid Mech.* **43**, 247–272.
- CHANDRA SEKAR, T., JAISWAL, K., ARORA, R., SUNDARARAJ, R.H., KUSHARI, A. & ACHARYA, A. 2021 Nozzle performance maps for fluidic thrust vectoring. *J. Propul. Power* **37**, 314–325.
- CHUE, S.H. 1975 Pressure probes for fluid measurement. *Prog. Aerosp. Sci.* **16**, 147–223.
- CODERONI, M., LYRINTZIS, A.S. & BLAISDELL, G.A. 2018 Les of unheated and heated supersonic jets with fluidic injection.
- CUPPOLETTI, D., GUTMARK, E., HAFSTEINSSON, H. & ERIKSSON, L.-E. 2014 The role of nozzle contour on supersonic jet thrust and acoustics. *AIAA J.* **52**, 2594–2614.
- CUPPOLETTI, D.R. & GUTMARK, E. 2014 Fluidic injection on a supersonic jet at various mach numbers. *AIAA J.* **52**, 293–306.
- DAVIS, M.R. 1982 Variable control of jet decay. *AIAA J.* **20**, 606–609.
- DRIFTMYER, R.T. 1972 A correlation of free jet data. *AIAA J.* **10**, 1093–1095.
- GUTMARK, E.J., SCHADOW, K.C. & YU, K.H. 1995 Mixing enhancement in supersonic free shear flows. *Annu. Rev. Fluid Mech.* **27**, 375–417.
- HENDERSON, B. 2010 Fifty years of fluidic injection for jet noise reduction. *Intl J. Aeroacoust.* **9**, 91–122.
- IBRAHIM, M.K., KUNIMURA, R. & NAKAMURA, Y. 2002 Mixing enhancement of compressible jets by using unsteady microjets as actuators. *AIAA J.* **40**, 681–688.
- JINDRA, K. 1970 Geometric effects on the performance characteristics of very small nozzles. Ohio School of Engineering.
- KATANODA, H., MIYAZATO, Y., MASUDA, M. & MATSUO, K. 2000 Pitot pressures of correctly-expanded and under-expanded free jets from axisymmetric supersonic nozzles. *Shock Waves* **10** (2), 95–101.
- KHAN, A., NAGESWARA RAO, A., BAGHEL, T., PERUMAL, A.K. & KUMAR, R. 2022 Parametric study and scaling of Mach 1.5 jet manipulation using steady fluidic injection. *Phys. Fluids* **34** (3), 036107.
- KNOWLES, K. & SADDINGTON, A.J. 2006 A review of jet mixing enhancement for aircraft propulsion applications. *Proc. Inst. Mech. Engrs G: J. Aerosp. Engng* **220**, 103–127.
- KROTHAPALLI, A., STRYKOWSKI, P. & KING, C. 1998 Origin of streamwise vortices in supersonic jets. *AIAA J.* **36**, 869–872.
- MILLER, S.A.E. & VELTIN, J. 2011 Experimental and numerical investigation of flow properties of supersonic helium-air jets. *AIAA J.* **49**, 235–246.
- MILLER, S.A.E., VELTIN, J., MORRIS, P.J. & MCLAUGHLIN, D.K. 2009 Assessment of computational fluid dynamics for supersonic shock containing jets. *AIAA J.* **47**, 2738–2746.
- MOFFAT, R.J. 1985 Using uncertainty analysis in the planning of an experiment. *J. Fluids Engng* **107** (2), 173–178.
- MUNDAY, D., GUTMARK, E., LIU, J. & KAILASANATH, K. 2011 Flow structure and acoustics of supersonic jets from conical convergent-divergent nozzles. *Phys. Fluids* **23** (11), 116102.
- MUPPIDI, S. & MAHESH, K. 2005 Study of trajectories of jets in crossflow using direct numerical simulations. *J. Fluid Mech.* **530**, 81–100.
- NEELY, A.J., GESTO, F.N. & YOUNG, J. 2007 Performance studies of shock vector control fluidic thrust vectoring.
- PANDA, J. 1998 Shock oscillation in under-expanded screeching jets. *J. Fluid Mech.* **363**, 173–198.
- PERUMAL, A.K. & RATHAKRISHNAN, E. 2013 Truncated triangular tabs for supersonic-jet control. *J. Propul. Power* **29**, 50–65.
- PERUMAL, A.K. & RATHAKRISHNAN, E. 2021 Scaling law for supersonic core length in circular and elliptic free jets. *Phys. Fluids* **33** (5), 051707.
- PERUMAL, A.K. & RATHAKRISHNAN, E. 2022 Design of fluidic injector for supersonic jet manipulation. *AIAA J.* **60**, 4639–4648.
- PERUMAL, A.K., VERMA, S.B. & RATHAKRISHNAN, E. 2015 Experimental study of subsonic and sonic jets controlled by air tabs. *J. Propul. Power* **31**, 1473–1481.

- PERUMAL, A.K., WU, Z., FAN, D. & ZHOU, Y. 2022 A hybrid AI control of turbulent jet: Reynolds number effect and scaling. *J. Fluid Mech.* **942**, 1–28.
- PERUMAL, A.K. & ZHOU, Y. 2018 Parametric study and scaling of jet manipulation using an unsteady minijet. *J. Fluid Mech.* **848**, 592–630.
- PERUMAL, A.K. & ZHOU, Y. 2021 Axisymmetric jet manipulation using multiple unsteady minijets. *Phys. Fluids* **33** (6), 065124.
- PERUMAL, K.A., ARAVINDH KUMAR, S.M., SURYA MITRA, A. & RATHAKRISHNAN, E. 2019 Empirical scaling analysis of supersonic jet control using steady fluidic injection. *Phys. Fluids* **31** (5), 056107.
- PHALNIKAR, K.A., KUMAR, R. & ALVI, F. 2008 Experiments on free and impinging supersonic microjets. *Exp. Fluids* **44**, 819–830.
- PHANINDRA, B.C. & RATHAKRISHNAN, E. 2010 Corrugated tabs for supersonic jet control. *AIAA J.* **48**, 453–465.
- POWELL, A. 1953 On the mechanism of choked jet noise. *Proc. Phys. Soc. B* **66**, 1039.
- RAO, A.N., KUSHARI, A. & MANDAL, A.C. 2020 Screech characteristics of under-expanded high aspect ratio elliptic jet. *Phys. Fluids* **32** (7), 076106.
- RATHAKRISHNAN, E. 2016 *Instrumentation, Measurements, and Experiments in Fluids*, pp. 368. CRC Press.
- SEIFERT, A., THEOFILIS, V. & JOSLIN, R. 2004 Issues in active flow control: theory, simulation and experiment. *Prog. Aerosp. Sci.* **40**, 237–289.
- SEMLITSCH, B., CUPPOLETTI, D.R., GUTMARK, E.J. & MIHĂESCU, M. 2019 Transforming the shock pattern of supersonic jets using fluidic injection. *AIAA J.* **57**, 1851–1861.
- SIROVICH, L. 1987 Proper orthogonal decomposition applied to turbulent flow in a square duct. *Q. Appl. Maths* **45**, 561–671.
- SMITH, T.D., CAIN, A.B. & CHENAULT, C.F. 2001 Numerical simulation of enhanced mixing in jet plumes using pulsed blowing. *J. Aircraft* **38**, 458–463.
- TAIRA, K., BRUNTON, S.L., DAWSON, S.T.M., ROWLEY, C.W., COLONIUS, T., MCKEON, B.J., SCHMIDT, O.T., GORDEYEV, S., THEOFILIS, V. & UKEILEY, L.S. 2017 Modal analysis of fluid flows: an overview. *AIAA J.* **55**, 4013–4041.
- TAM, C.K.W., SEINER, J.M. & YU, J.C. 1986 Proposed relationship between broadband shock associated noise and screech tones. *J. Sound Vib.* **110**, 309–321.
- WARSON, C. & CROWTHER, W.J. 2018 Fluidic flow control effectors for flight control. *AIAA J.* **56**, 3808–3824.
- WERLE, M.J., SHAFFER, D.G. & DRIFTMYER, R.T. 1970 On freejet terminal shocks. *AIAA J.* **8**, 2295–2297.
- WU, K., KIM, T.H. & KIM, H.D. 2020 Theoretical and numerical analyses of aerodynamic characteristics on shock vector control. *J. Aerosp. Engng* **33** (5), 04020050.
- ZAMAN, K.M.Q., REEDER, M.F. & SAMIMY, M. 1994 Control of an axisymmetric jet using vortex generators. *Phys. Fluids* **6** (2), 778–793.
- ZHANG, H., AUBRY, N., CHEN, Z., WU, W. & SHA, S. 2019 The evolution of the initial flow structures of a highly under-expanded circular jet. *J. Fluid Mech.* **871**, 305–331.
- ZHANG, L. & FAN, J. 2003 Research of optimized design of three-dimensional contraction. *Acta Aeronaut. Astronaut. Sin.* **21**, 417–423.
- ZIGUNOV, F., SONG, M., SELLAPPAN, P. & ALVI, F.S. 2022 Multiaxis shock vectoring control of overexpanded supersonic jet using a genetic algorithm. *J. Propul. Power* **39** (2), 249–257.
- ZUCROW, M. & HOFFMAN, J. 1976 *Gas Dynamics*. Wiley.